MODELLING ROTATION CURVES IN MARGINALLY RESOLVED WARPED GALAXIES

LA MODÉLISATION DE COURBES DE ROTATION DANS DES GALAXIES TORDUES À BASSE RÉSOLUTION

A Thesis Submitted to the Division of Graduate Studies
of the Royal Military College of Canada
by

Alex Gasser, BSc
Captain

In Partial Fulfillment of the Requirements for the Degree of
Master of Science in Physics

May, 2023

Acknowledgements

First and foremost, I would like to thank my thesis supervisor, Dr. Kristine Spekkens, for all the knowledge and experience she brought to this project and for her mentorship. Second, I would like to thank Dr. Nathan Deg for the numerous analysis recommendations and programming support he has provided. Third, I would like to thank my committee, for taking time out of their busy schedules to examine my thesis. And last but not least, I would like to thank my lovely wife, Marie, for her support, and for taking care of our daughter while I was typing this very text. Without you the completion of this thesis would not have been possible.

Abstract

Early statistical studies indicate that roughly 50 - 70% of spiral galaxies contain visible warps. Neutral hydrogen surveys from the Square Kilometer Array (SKA) pathfinders, such as WALLABY on the Australian Square Kilometer Array Pathfinder (ASKAP) telescope, will image hundreds of thousands of galaxies; increasing the number of catalogued HI galaxies by an order of magnitude. Most detections will be marginally spatially resolved, with fewer than 15 beams across their major axes (N_{beam}). Inevitably, many of them will be warped. Surveys of this nature make use of modelling tools in order to better understand galaxy parameters and ultimately to further our knowledge of the universe. These tools have, however, not been tested under all conditions. In this thesis, we test the Fully Automated TiRiFiC (FAT) kinematic modelling algorithm's ability to recover the rotation curves of marginally resolved warped galaxies and determine the impacts of fitting flat disk models to intrinsically warped galaxies.

We first create a set of mock observations of flat-disk galaxies in order to determine the minimum spatial resolution, HI mass (M_{HI}) and inclination(i) required for FAT to reliably recover the mock galaxy's rotation curve. We then generate 500 WALLABY-like observations to test these limits on a wider range of parameters. We find that FAT can accurately recover the rotation curves of galaxies with $M_{HI} \geq 8$ dex $M/M_{\odot}$ if a) their $N_{beam} \geq 2$ and $i \geq 65°$; or b) their $N_{beam} \geq 5$ and $i \geq 50°$.

Then, we generate 500 WALLABY-like observations of warped galaxies and fit models to them using FAT. We find that FAT accurately determines the rotation curve at similar parametric values as for flat disks; however, it often fails to recognize the presence of a warp.

Lastly, we force FAT to fit flat models to warped mock galaxies. We find very little difference in FAT's ability to recover the rotation curves, thus concluding that for widefield surveys similar in depth and resolution to WALLABY it is acceptable to fit flat disk models to warped galaxies. This result is strictly valid for the symmetric warps in the idealized mock galaxies studied

here.

Résumé

Les études statistiques indiquent qu'environ 50 à 70% des galaxies de type spirale contiennent des distorsions dans leur disque visible. Les collectes de données sur l'hydrogène neutre menées par les précurseurs du Square Kilometer Array (SKA), telles que WALLABY sur le télescope australien Australian Square Kilometer Array Pathfinder (ASKAP), permettront d'imager des centaines de milliers de galaxies; augmentant ainsi considérablement le nombre de galaxies HI cataloguées. La plupart de ces détections seront marginalement résolues spatialement, avec moins de 15 faisceaux sur leurs axes majeurs (N_{beam}). Inévitablement, beaucoup d'entre elles seront déformées. Les enquêtes de cette nature utilisent des outils de modélisation pour mieux comprendre les paramètres des galaxies et, en fin de compte, pour approfondir nos connaissances sur l'univers. Cependant, ces outils n'ont pas été testés dans toutes les conditions. Dans cette thèse, nous testons la capacité de l'algorithme de modélisation cinématique Fully Automated TiRiFiC (FAT) à récupérer les courbes de rotation des galaxies déformées marginalement résolues et déterminons les impacts d'utiliser des modèles à disque plat aux galaxies intrinsèquement déformées.

Pour ce faire, nous créons d'abord un ensemble d'observations fictives de galaxies à disque plat qui sont de plus en plus difficiles à modéliser cinématiquement afin de déterminer la performance de FAT dans le régime marginalement résolu. Nous générons ensuite 500 observations similaires à celles que prendra WALLABY pour tester ces limites sur une plage de paramètres plus large. Nous constatons que FAT peut récupérer avec précision les courbes de rotation des galaxies avec des masses HI $\geq 8\,dex\,M/M_{\odot}$ si a) leur $N_{beam} \geq 2$ et $i \geq 65°$; ou b) leur $N_{beam} \geq 5$ et $i \geq 50°$.

Ensuite, nous générons 500 observations fictives de galaxies déformées similaires à celles que prendra WALLABY et créons des modèles cinématiques de ceux-ci à l'aide de FAT. Nous constatons que FAT détermine avec précision la courbe de rotation à des valeurs paramétriques similaires à celles des disques plats, mais ne réussit souvent pas à reconnaître la présence d'une déformation.

Enfin, nous forçons FAT à créer des modèles plats des galaxies fictives déformées. Nous constatons très peu de différences dans la capacité de FAT à récupérer la courbe de rotation, concluant ainsi que pour les collectes de données de grandes parties du ciel, similaires en profondeur et en résolution à WALLABY, il est acceptable d'utiliser des modèles de disque plat pour représenter des galaxies déformées. Ce résultat est strictement valide pour les déformations symétriques dans les galaxies fictives idéalisées étudiées ici.

Contents

List of Tables

List of Figures

List of Symbols

c	speed of light (3×10^8 m s^{-1})
D	diameter
i	inclination
r	radius
z	redshift
D_{HI}	diameter at which the HI column density drops below $1\,\mathrm{M}_\odot\,\mathrm{pc}^{-2}$
Inc_{end}	value of the inclination at $r = 1.5\,R_{HI}$ in the warped mock galaxies created in MCG
M_{HI}	HI mass
$M_\odot$	solar mass
N_{beam}	number of beams across the major axis
PA_{end}	value of the position angle at $1.5\,R_{HI}$ in the warped mock galaxies created in MCG
r_w	warp radius
$R_{warpstart}$	warp radius as implemented in MCG
R_{Ho}	Holmberg radius
R_{HI}	radius at which the HI column density drops below $1\,\mathrm{M}_\odot\,\mathrm{pc}^{-2}$
R_{25}	radius at which the surface brightness reaches 25.0 mag arcsec^{-2}
V_{rot}	rotational velocity
V_{sys}	systemic velocity
α	warp angle as measured between the center of the galaxy and the outer most isophote
β	warp angle as measured from the onset of the warp to the outer most isophote
δ	declination
λ	wavelength
ν	frequency
Θ_0	angular resolution

List of Acronyms

ALFA	Arecibo L-Band Feed Array
ALFALFA	Arecibo Legacy Fast ALFA Survey
APERTIF	APERture Tile In Focus
ASKAP	Astralian Square Kilometer Array Pathfinder
DEC	Declination
FAT	Fully Automated TiRiFiC
FITS	Flexible Image Transport System
FWHM	Full Width Half Maximum
HERA	Hydrogen Epoch of Reionization Array
HI	Neutral Hydrogen
HIPASS	HI Parkes All Sky Survey
LOFAR	Low Frequency Array
LVHIS	Local Volume HI Survey
MCG	Mock Cube Generator
MWA	Murchison Widefield Array
PA	Position Angle
PDR1	Pilot Data Release 1
RA	Right Ascension
SKA	Square Kilometer Array
SMBH	Super Massive Black Hole
SOFIA	Source Finding Application
TiRiFiC	Tilted Ring Fitting Code
WALLABY	Widefield ASKAP L-band Legacy All-sky Blind surveY
WKAPP	WALLABY Kinematic Analysis Proto-Pipeline
WSRT	Westerbork Synthesis Radio Telescope

Chapter 1

Introduction

Astronomical sciences originated far before other natural sciences such as physics and chemistry. In a remote past, astronomy played a role not only on a scientific level but also on a cultural level: it was the origin of many tales and prophesies (Pannekoek, 1989). Over time the study of the moon, planets, stars and ultimately galaxies that surround us led to our understanding of the universe. We now know that the Milky Way in which we live is an agglomeration of gravitationally-bound gas, stars, dust and dark matter, and that it is a galaxy like many others in the universe. This, however, is not all there is to know. With the technological advances being made, we can probe deeper into these systems and with a better resolution than ever before, allowing a better understanding of galaxy formation and evolution.

1.1 Anatomy of a Galaxy

It is generally accepted amongst astronomers that there are three basic types of galaxies: spiral (or disk), elliptical and irregular. All three types contain a mixture of gas, stars, dust and dark matter, albeit in different proportions, and are thought to contain a supermassive black hole (SMBH) at their center.

Disk galaxies are active in star formation and are predominant in the local universe. They get their name from the fact that their stars and gas reside on a relatively flat disk and their orbits create spiral arms. Elliptical galaxies contain older stars and, generally, no longer actively form stars. They can be nearly circular or very elongated and vary widely in size, with many being so-called Dwarf galaxies. When in dense environments, the dominant galaxy is often an elliptical galaxy typically larger than its neighbouring disk galaxies. The stellar motions are random in elliptical galaxies, thus their stars are not confined to a plane. Irregular galaxies are those that do not have

any particular shape. Some such galaxies seem to be in a transitory phase of galactic evolution, such as interacting with a neighbour or undergoing collision. Many irregular galaxies can be found in the distant universe. In this thesis, we will analyse rotation curves of disk galaxies. We will discuss rotation curves later, but first let's discuss the structure of disk galaxies.

The main components of a disk galaxy are as follows:

1. A SMBH at its core;
2. A stellar bulge;
3. A stellar disk;
4. Gaseous disks; and
5. A dark matter halo.

The components that shine in visible light can be seen in Figure 1.1. The SMBH is a region of extremely compact matter, where even light cannot escape gravitational attraction. It is not distinguishable in the figure, as it is embedded in the bulge. The stellar bulge is a region composed of stars with orbits of arbitrary direction of motion. In the figure, it can be distinguished as the spherical region near the center of the galaxy. The stellar and gaseous disks are regions where the stars and gases are largely in circular orbits in the dark matter potential well. The dark matter potential well dominates the mass budget. Its center coincides with the center of the visible components, giving the impression that the stars and gases rotate around the visible center. This rotation puts a force on the gases, which collapse in order to conserve angular momentum, resulting in a flat structure. The stars and gases, do however maintain a certain thickness about the plane.

Many different types of gas disks are present in a galaxy. Of importance to this thesis is the neutral hydrogen disk, which extends far beyond the stellar disk. The stellar disk is represented in the image as the flat, extended disk. The neutral hydrogen disk cannot be seen as it does not emit in the visible spectrum. Finally, the dark matter halo is a hypothesised spherical structure that envelops all other components of the galaxy. It is thought to extend far beyond all baryonnic components. It gets its name from the fact that it emits very little to no electromagnetic radiation and therefore cannot be observed.

The disks of spiral galaxies may exhibit other features such as bars or warps. Bars are stellar structures deviating from the regular rotational motion in a galaxy. They are instabilities that develop in the disk due to a combination of the disk's self-gravity and the overall gravitational potential (Elmegreen and Elmegreen, 1985). Warps can be seen as material deviating from the plane

of the disk (Binney, 1992). Their formation mechanism is still under debate; a more in depth description and current hypotheses for their formation will be discussed in section 2.2. Warps are common in the outskirts of atomic gas disks and can sometimes be seen in the stellar disk. Bars and warps in a stellar disk can be seen in Figure 1.2.

When it comes to observing disk galaxies, the inclination (i) and position angle (PA) have large effects on what is observed. i is the angle between the sky plane and the plane of the disk. A galaxy with $i = 0°$ is referred to as being face-on, while a galaxy with $i = 90°$ is considered edge-on. The PA is the sky-plane angle to the projected disk major axis, measured North - East. Figure 1.3 shows a visual representation of i and PA. Panels a) through d) show the neutral hydrogen content of a mock galaxy at PA,i = (0°,0°), (0°,90°), (0°,45°), (45°,45°).

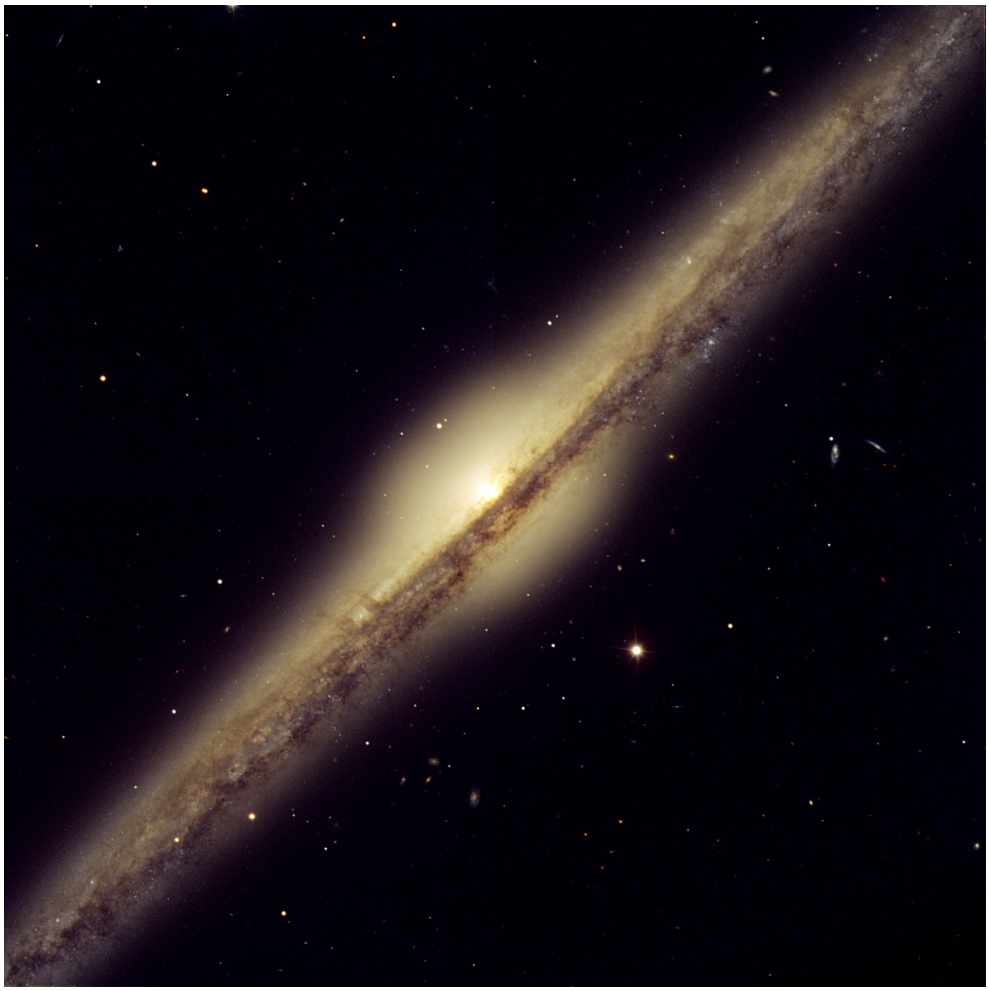

Figure 1.1: A true-colour optical image of NGC 4565 (the Flying Saucer Galaxy), an edge-on disk galaxy in Coma Berenices. The stellar bulge can be seen as the spherical portion near the center of the galaxy, while the stellar disk can be seen as the extended flat disk. Image credit: ESO

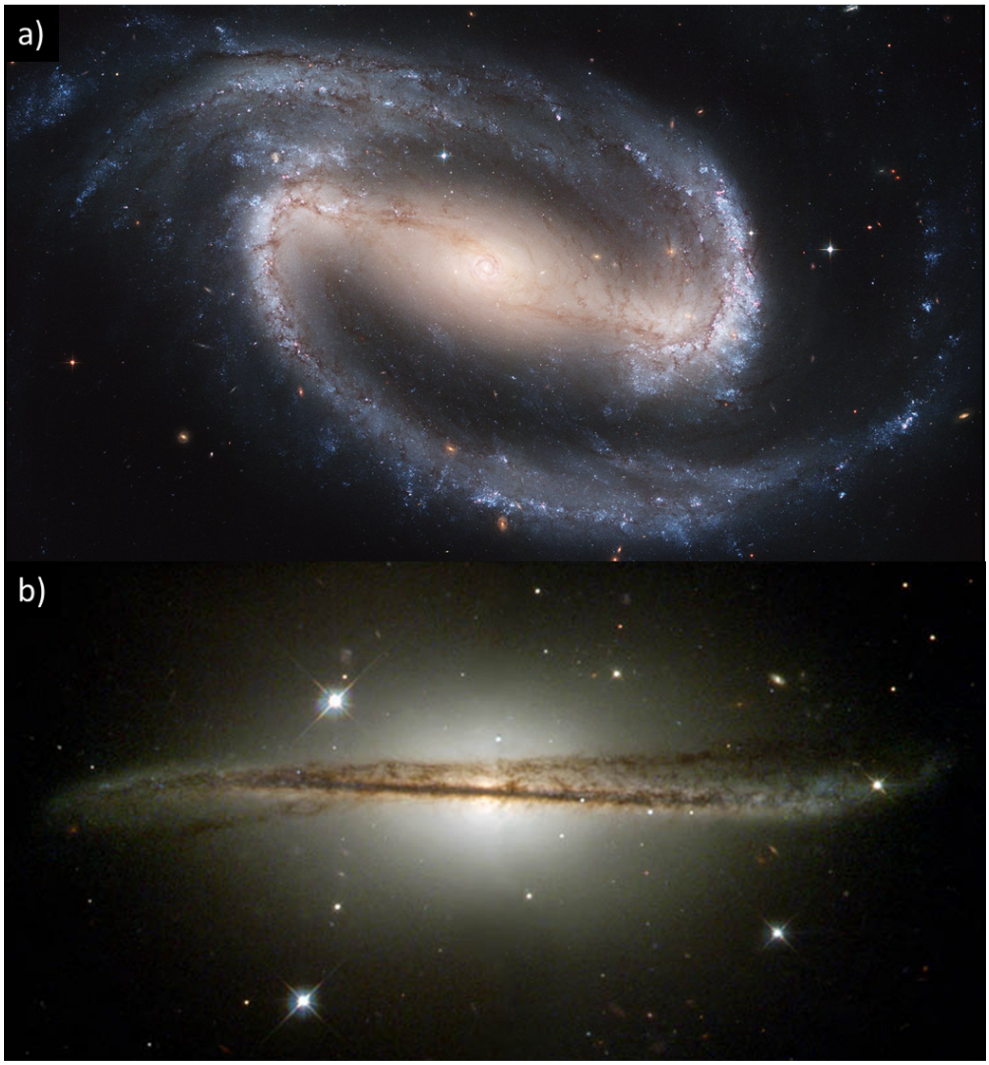

Figure 1.2: Barred galaxy NGC 1300 (panel a) and warped galaxy ESO 510-G13 (panel b) as imaged by the Hubble Space Telescope. Image credit: NASA, ESA, and The Hubble Heritage Team.

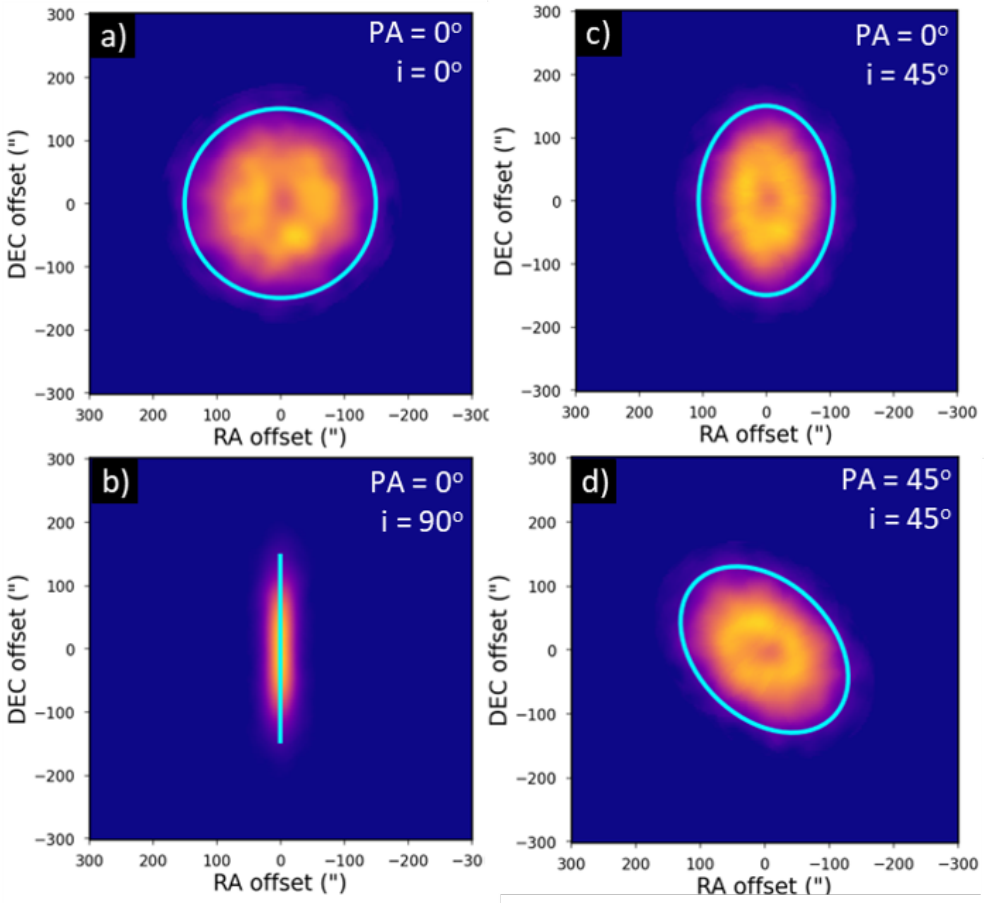

Figure 1.3: False-colour images of a mock HI disk projected at PA,i = (0°,0°), (0°,90°), (0°,45°), (45°,45°). The axis units of offset in Right Ascension (RA) and declination (DEC, δ) are relative to the galaxy center. The cyan line depicts the galaxy's HI size as defined by D_{HI} (the diameter at which the HI column density drops below $1\,\mathrm{M}_\odot\,\mathrm{pc}^{-2}$). Image created using the MCG and MS PowerPoint software.

1.2 Rotation Curves and Neutral Hydrogen

In disk galaxies, the stellar and gaseous disks rotate circularly around the galactic center. The velocity of the stars and gases can be measured, and when plotted as a function of radius, we obtain what astronomers call a rotation curve. Rotation curves have allowed astronomers to discover that the gas and stars composing the galaxy do not rotate as expected if the baryonic material in the disk is the only gravitating mass. Indeed, if this were the case, we would expect the rotational velocity to decrease as radius increases. This is not what is observed; rather the rotational speed of the gas on the outskirts of the galaxy often remains constant or continues to increase. This is sometimes referred to as the "missing mass" problem, as in order to explain the observed rotation curve additional mass must be present in the galaxy. This is one of the phenomena that lead to the theory of dark matter. The dark matter mass profile can be determined by comparing the observed rotation curve to that expected from a purely luminous matter galaxy. In combination with mass estimates for the various baryonic matter, such as stellar mass ($M_\odot$), neutral hydrogen (HI) mass (M_{HI}), etc. one can produce a complete mass profile for a galaxy.

One of the best observational tools available for this purpose is the emission line of neutral hydrogen: the 21 cm line. This spectral line is often referred to as HI (pronounced H-one) line by astronomers. When a ground state neutral hydrogen atom's electron's spin transitions from aligned with its nucleus to anti-aligned, a photon with a rest frequency of 1420 MHz is emitted. This frequency is analogous to a wavelength of 21 cm. This process is quantum mechanically forbidden and therefore has an extremely low probability of occurring for a given atom, however, the sheer amount of hydrogen in galaxies makes this spectral line readily observable. Furthermore, neutral hydrogen is the gas that extends furthest from a galaxy's center. When measured in HI, the size of a galaxy is defined by its neutral hydrogen diameter (D_{HI}), which is the diameter at which the HI column density drops below $1\,M_\odot\,pc^{-2}$. The galaxy's spatial resolution is measured in number of beams that fit in D_{HI} (N_{beam}), where a "beam" refers to the Full Width Half Maximum (FWHM) of the telescope's beam. This is the width at which half the power is received by the antenna. The beam (or beam size) is therefore a measure of the point-spread function, or impulse response, of the telescope.

Figure 1.4 shows the extent of HI gas as compared to stars for M74. Thus by observing in HI, one can generate a rotation curve that extends far beyond the stellar disk. Figure 1.5 shows the expected rotation curve for M33 if it did not contain dark matter (grey dashed line) and the observed rotation curve

using both stellar and HI observations (solid white line).

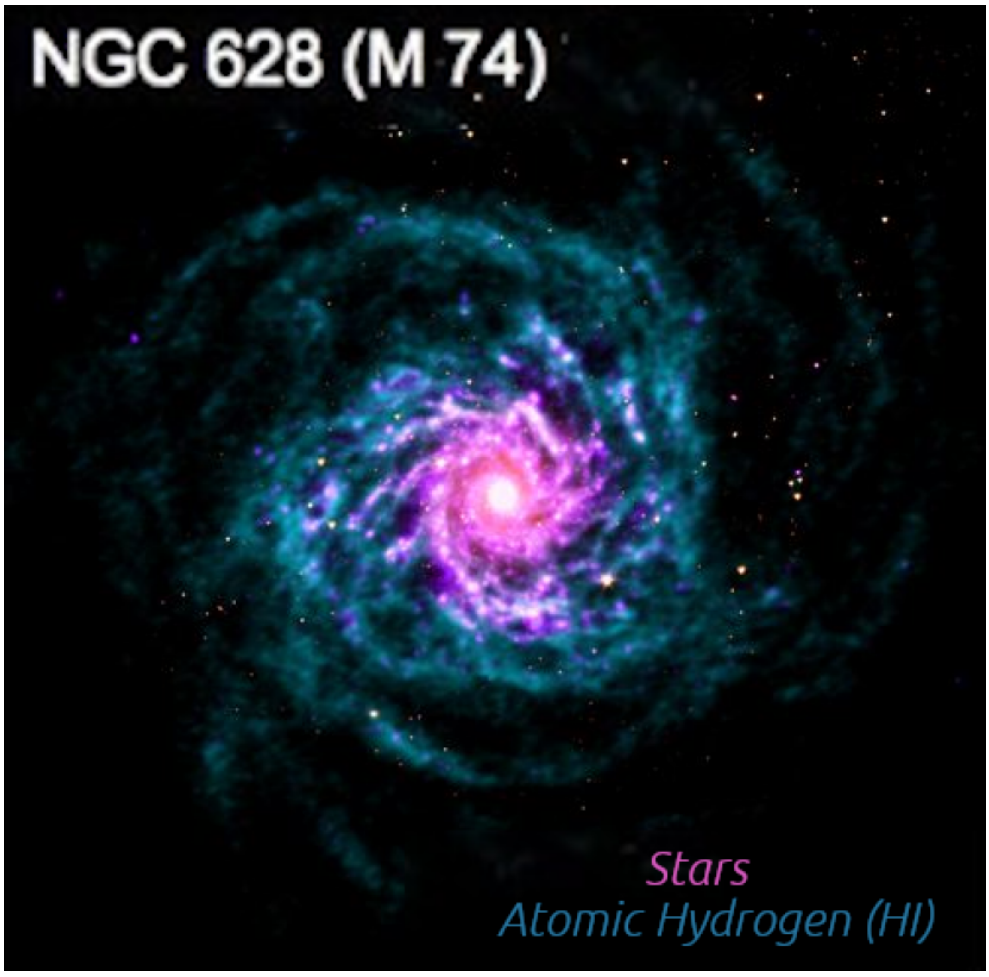

Figure 1.4: False colour image of M74 with overlaid observations of HI gas (blue) and stars (pink). Image credit: Walter et al. (2008); Lewis (2019)

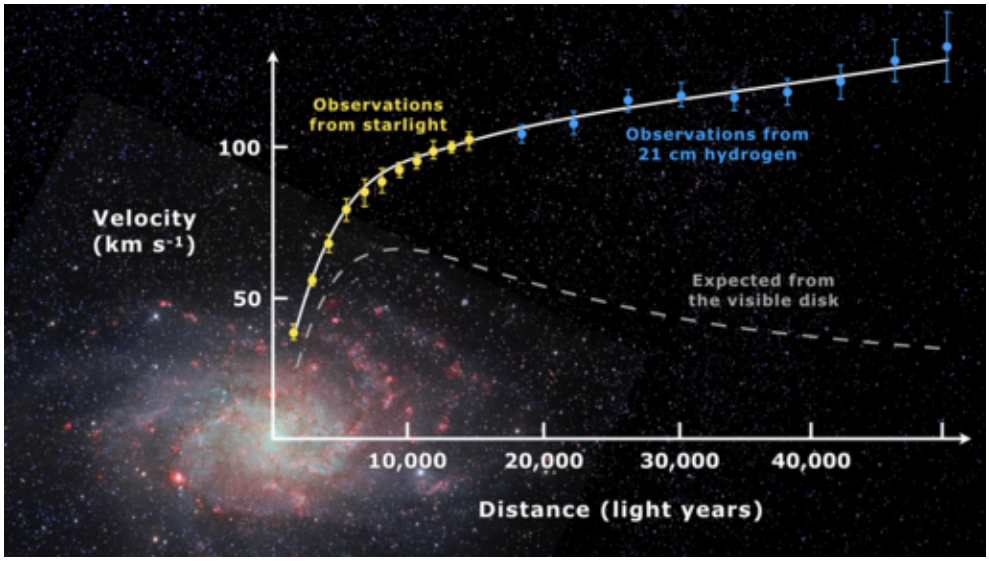

Figure 1.5: Rotation curve of galaxy M33, showing the expected rotational velocity if there were no dark matter (dashed grey line) and the measured rotational velocity (solid white line). Observed velocities are separated in stellar light (yellow data points) and in 21cm light (blue data points). Image credit: Mario De Leo, via Wikimedia Commons.

1.3 Radio interferometers and HI surveys

Rotation curves made from HI observations are extremely useful probes of dark matter distribution. However, creating rotation curves for a large quantity of galaxies, within a reasonable amount of time, has only become feasible in recent years. As previously mentioned, the photon emitted by the hydrogen spin flip process has a rest frequency of 1420 MHz. This falls in the radio spectrum of light, therefore a radio telescope is needed to make these observations.

Large sky untargetting HI surveys on single dish telescopes have been conducted several times in the past. For example there was the HI Parkes All Sky Survey (HIPASS, Zwaan et al. 2004) and the Arecibo Legacy Fast ALFA Survey (ALFALFA; of which ALFA stands for Arecibo L-Band Feed Array, Haynes et al. 2018). HIPASS detected 4,135 HI sources, at $\delta < 2^\circ$ (Zwaan et al., 2004), while ALFALFA detected ∼31,500 extra-galactic HI line sources (Haynes et al., 2018). These surveys tremendously helped the advancement of science, despite having a lower resolution than that of new interferometers such as the future Square Kilometer Array (SKA) and its pathfinders. HIPASS had a spatial resolution of $\sim 14'.3$ (arcminutes, equivalent to $1/60^\circ$) (Barnes et al., 2001), while ALFALFA had a spatial resolution of $\sim 3'.5$ (Giovanelli et al., 2005). In comparison, the Australian Square Kilometer Array Pathfinder (ASKAP) will have a spatial resolution of $30''$ (arcseconds, equivalent to $1/3600^\circ$).

An important feature of radio telescopes is that their angular resolution is limited by diffraction:

$$\theta_0 = 1.22\frac{\lambda}{D} \tag{1.1}$$

where θ_0 is the angular resolution (in radians), λ is the observed wavelength and D is the diameter of the telescope. Therefore if one wanted to observe a galaxy in HI with an angular resolution of $30''$, even to resolve many nearby galaxies, one would need a telescope with a diameter of $\sim 1760\,\mathrm{m}$. Creating a single dish of this size is not feasible. Luckily, one can build a radio interferometer to achieve such a resolution.

Radio interferometers, like ASKAP (see Figure 1.6) use two or more correlated radio receivers separated by a baseline distance to observe a target simultaneously. This allows the telescope to have a spatial resolution equivalent to that of a single dish with a diameter equal to the baseline distance. Note however that the light gathering power of an interferometer does not increase in the same way, meaning that large integration times are needed for fainter galaxies. For that reason, in the early days of radio astronomy, interferometers were largely used to observe bright objects at high resolution.

Figure 1.6: Dishes of the Australian Square Kilometre Array Pathfinder (ASKAP) © Kim Steele

1.4 The Square Kilometer Array and WALLABY

Square Kilometer Array

The SKA is a state of the art observatory for which construction was divided in two phases: SKA1 and SKA2. The full scope of SKA2 is still under discussion and will therefore not be mentioned here. Furthermore, SKA1 will simply be referred to as SKA for the remainder of this paper as is often done in current literature.

The construction of the SKA began in December 2022 with a planned completion date of July 2029. It will be composed of two radio telescopes: SKA-Low and SKA-mid, which will be located in Australia (at the Murchison Radio-astronomy Observatory) and South Africa (in the Karoo desert), respectively. SKA-Low will be composed of 512 aperture array stations each containing 256 antennas. SKA-Low will operate in the 50-350 MHz range. SKA-Mid will consist of 133 15 m SKA dishes and 64 13.5 m Meerkat dishes. SKA-mid will operate in four different bands: 350 - 1050 MHz, 950 - 1760 MHz, 4600 - 8500 MHz and 8300 - 15300 MHz, with possible upgrades covering other bands (McMullin et al., 2022).

The SKA will be the next great science instrument. Astronomers are very excited for its construction to be complete and to start collecting data with it. However, there are still several years to wait. In the meantime its precursors are being used both for science and as a testing bed for the future SKA instruments. As with many other science instruments, the SKA has

been designed with the knowledge acquired by its precursors: MeerKAT, the Hydrogen Epoch of Reionization Array (HERA), the Murchison Widefield Array (MWA), the Australian Square Kilometer Array Pathfinder (ASKAP, McMullin et al. 2020), the APERture Tile In Focus (APERTIF) technology installed on the Westerbork Synthesis Radio Telescope (WSRT, Adams et al. 2018) and the Low Frequency Array (LOFAR, Röttgering 2003). All of which are currently being used to test crucial new equipment that will be part of the future SKA, while simultaneously gathering scientific data. Of pertinence to this paper is ASKAP's Widefield ASKAP L-band Legacy All-sky Blind surveY (WALLABY, Koribalski et al. 2020).

WALLABY on ASKAP

ASKAP is a radio telescope array located in western Australia, that uses 36 12 meter wide dish antennas to image the radio sky. It was designed as a widefield survey instrument and can provide extremely large amounts of data in record breaking time (Koribalski et al., 2020). ASKAP uses a phased-array feed technology which gives it a large field of view ($30\,\mathrm{deg}^2$ per antenna), making it an excellent untargetted surveying instrument.

WALLABY will survey 3/4 of the entire sky in HI with a resolution of $30''$. It is expected that, once completed, WALLABY will have detected half a million galaxies and will have increased the number of catalogued HI galaxies by an order of magnitude. Furthermore, it will provide well resolved HI maps for $\sim$ 5000 nearby galaxies (Koribalski et al., 2020). The majority of these detections, will however be in the marginally resolved regime. Figure 1.7 shows the number of detections as a function of angular size for the observations presented in the WALLABY Pilot Data Release 1 (PDR1) paper (Westmeier et al., 2022). In Figure 1.7, the spatial resolution is determined by the Source Finding Application (SOFIA) (Serra et al., 2015), often referred to as the SOFIA "ell_maj". The SOFIA ell_maj is a factor of $\sim$ 2 smaller than the spatial resolution as defined by D_{HI} (Deg et al., 2022). When looking at Figure 1.7, we should therefore multiply the values on the x axis by 2 to normalize to the values that will be used throughout this thesis.

From this figure, we can see that a majority of the detections are marginally resolved with $2 < N_{beam} < 6$ and a significant number of galaxies are resolved at $6 < N_{beam} < 15$. We have therefore set the resolution limits of our tests to $2 < N_{beam} < 15$.

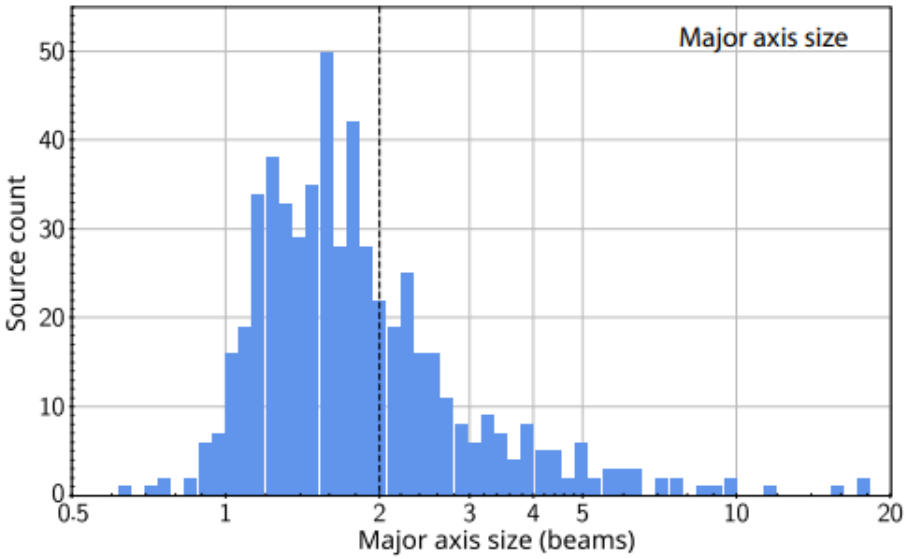

Figure 1.7: Histogram of the galaxies detected by WALLABY's pilot data release 1 (PDR1) as a function of spatial resolution. Image credit: Westmeier et al. (2022).

1.5 Data Cubes, Kinematic models and Warps

When a radio telescope, such as ASKAP, takes an image of a galaxy, it generates a data cube. A data cube can be though of as a container containing 3 dimensions of information. In this case, the container has two spatial dimensions and one frequency dimension. The spatial dimensions represent the right ascension and declination in the sky (where the telescope is pointing), while the frequency dimension gives the frequency at which the light was observed. The rest frequency of neutral hydrogen is 1420 MHz, however the observed frequency will vary about this value following the Doppler equation. This variation in frequency can be used to determine how fast the galaxy is moving away from us as a whole (its systemic velocity (V_{sys})) or how parts of the galaxy are moving intrinsically in the line of sight. Any movement perpendicular to the line of sight will not be reflected in a change in frequency, and hence cannot be determined directly.

Observed data cubes can be used to generate kinematic models: models describing the movement (including the rotation curve) and structure of a galaxy. One way to test a kinematic modelling tool's performance is to build mock observations, for which the galaxy parameters are known and have the kinematic modelling tool generate a model for this mock observation. In doing

so, the generated model can be compared to the true value in order to determine the tools performance. This technique has been done many times in the past, however was never performed on a large sample of warped galaxies. We know HI disks are often warped (García-Ruiz et al., 2002), but despite this, flat disk models are used to describe galaxies in untargetted surveys. It is unclear whether a warped galaxy's rotation curve can be properly described by a flat model.

1.6 This Thesis

With the arrival of new modern radio telescopes such as the SKA and its precursors, an unprecedented amount of data will be collected. It is planned that hundreds of thousands of new galaxies will be discovered. Kinematic models for these galaxies will be required, making an automatic modelling tool indispensable. Such tools already exist, however they have not been tested for all conditions. In this thesis, we will test the Fully Automated TiRiFiC's (FAT) (Kamphuis et al., 2015) ability to recover the rotation curve of marginally resolved galaxies, and of marginally resolved warped galaxies; and we will test whether the rotation curve is well recovered when fitting a flat disk model to a warped galaxy.

The structure of the thesis is as follows. In Chapter 2 we present a literature review, focusing on the statistical analysis of warps, on WALLABY, and on the software used throughout this thesis. In Chapter 3, we evaluate FAT's ability to recover the rotation curve of marginally resolved flat galaxies in a similar manner than has been done by Lewis (2019). In Chapter 4, we evaluate the algorithm's performance on marginally resolved warped galaxies and determine the effects of fitting a flat model to a warped galaxy. Finally, in Chapter 5, we summarize our findings and recommend future work.

Chapter 2

Literature Review

In this chapter, we will discuss WALLABY in detail, review studies on the statistical properties of warped galaxies and give an overview of the programmes used throughout the rest of this thesis. In section 2.1, we present the WALLABY survey and describe some science that has been performed with its early results. In section 2.2, we present previous studies on warps, focusing on their frequency and strength and we review theories for their formation. In section 2.3, we discuss tilted ring modelling. In sections 2.4 and 2.5 we cover the basic functions and processes of the Fully Automated TiRiFiC (FAT) and the Mock Cube Generator (MCG). Finally, in section 2.6, we discuss the goals of this thesis and its structure.

2.1 WALLABY

As introduced in chapter 1, the Widefield ASKAP L-band Legacy All-sky Blind surveY (WALLABY) is a neutral hydrogen survey, conducted on the Australia Square Kilometer Array Pathfinder (ASKAP) telescope. The survey intends to image 3/4 of the entire sky ($-90° \leq \delta \leq +30°$) at a spatial resolution of 30", spectral resolution of $4\,\mathrm{km\,s^{-1}}$ and channel sensitivity of 1.6 mJy $\mathrm{beam^{-1}}$ (Koribalski et al., 2020). A full list of survey parameters can be found in Table 2.1.

2.1.1 ASKAPs Phased-Array Feed

Single dish radio telescopes use specialised cameras, called receivers, to detect and amplify faint radio waves from space. Their angular resolution is limited by the size of the dish as per equation 1.1. Interferometers are a type of radio telescope that use multiple correlated radio receivers that simultaneously ob-

Table 2.1: WALLABY Survey parameters; modified table from Koribalski et al. (2020).

Parameter	Value
telescope	ASKAP
baseline	22 m to $\sim$ 2 km
Field of view	$\sim 30\,\mathrm{deg}^2$
angular resolution	$\sim$ 30"
sky coverage	$\delta < +30°$
frequency coverage	1130 - 1430 MHz
velocity range	-2 000 to + 77 000 $\mathrm{km\,s^{-1}}$
	$z \leq 0.26$
no. of channels	16 200
channel width	$\sim 4\,\mathrm{km\,s^{-1}}$
velocity resolution	$\sim 4\,\mathrm{km\,s^{-1}}$
rms per channel	$\sim 1.6\,\mathrm{mJy\,beam^{-1}}$
expected HI detections	$\sim$ 500 000

serve the sky. This allows the telescope to have an increased spatial resolution. Receivers from most single dish radio telescopes and traditional interferometers only see a small part of the sky at once, making surveying large parts of the sky a time-consuming process. ASKAP is unique in that it uses a new technology called "phased-array feeds". This technology consists in having 188 individual receivers positioned in a chequerboard-like arrangement at the focal point of each of the 36 antennas (Hotan et al., 2021; Chippendale et al., 2010). Together with specialised digital systems developed for ASKAP, the phased array feeds create 36 separate (simultaneous) beams to give a field-of-view of 30 deg^2 on the sky. This extremely large field of view enables large sky surveys like WALLABY to be completed faster than ever before.

2.1.2 Early Science

The first pilot data release (PDR1) from WALLABY presented observations for nearly 600 galaxies (Westmeier et al., 2022). The wide-field, higher-resolution HI view of galaxy groups and clusters enabled a variety of new scientific studies. Some early studies include: an HI study of the NGC 7162 galaxy group (Reynolds et al., 2019); an HI study of the NGC 7232 galaxy group (Lee-Waddell et al., 2019); an HI study of spiral galaxy NCG 1566 (Elagali et al., 2019); HI imaging of the nearby galaxy IC 5201 (Kleiner et al., 2019); HI imaging of the Lyon Group of Galaxies 351 (For et al., 2019); the

detection of two low surface brightness HI clouds in the vicinity of NGC 1395 (Wong et al., 2021); the creation of the WALLABY Kinematic Analysis Proto-Pipeline (WKAPP, Deg et al. 2022); and the creation of HI kinematic models for over 100 galaxies from phase 1 of ASKAP pilot observations (Deg et al., 2022). Many more such studies are currently being carried out and new papers are coming out on a regular basis. In the mentioned studies, it was found that galaxies NGC 1566 and IC 5201 have warped HI disks.

2.2 Galactic Warps

2.2.1 Warp Characteristics

Briggs (1990) observed high quality HI data of 12 warped galaxies and defined a set of "Rules of behaviour for galactic warps". These rules are:

1. The warp develops between R_{25} (where the surface brightness reaches 25.0 mag arcsec^{-2}) and the Holmberg radius, R_{Ho} (where the surface brightness reaches 26.5 mag arcsec^{-2});

2. The line of nodes tends to be straight within R_{Ho}; and

3. Outside R_{Ho}, the line of nodes curves to form a spiral.

Since 1990, many new analyses were conducted on populations of warped galaxies. Despite this, the above "rules of behaviour for galactic warps" still hold true today. In addition to these rules, it has been found that in many cases, but not all, there is a sharp truncation in the HI radial surface brightness profile (Van der Kruit, 2007; Kregel et al., 2002). When this is the case, the rotation curve often shows a decline at the truncation radius, indicating that both the light and mass are truncated (Van der Kruit, 2007). Additionally, many warps were found to have a wiggle, where the stars and dust first move in one direction then in the other (Ann and Park, 2006). An example of a galaxy with an HI warp can be seen in Figure 2.1.

Early statistics on the frequency of optical warps indicate that 50 to 70% of disk galaxies contain a visible stellar warp (Sanchez-Saavedra et al., 1990; Reshetnikov and Combes, 1998). In their respective papers, Ann and Park (2006) identified 236/325 galaxies as containing a warp; García-Ruiz et al. (2002) identified 20/26; and Sánchez-Saavedra et al. (2003) identified 150/276. The high proportion of galaxies that contain a warp in the optical in combination with the fact that warps start near the end of the optical disk suggests that almost all galaxies contain a warp. García-Ruiz et al. (2002) even go as far as to say that every time a galaxy has an extended HI disk with respect

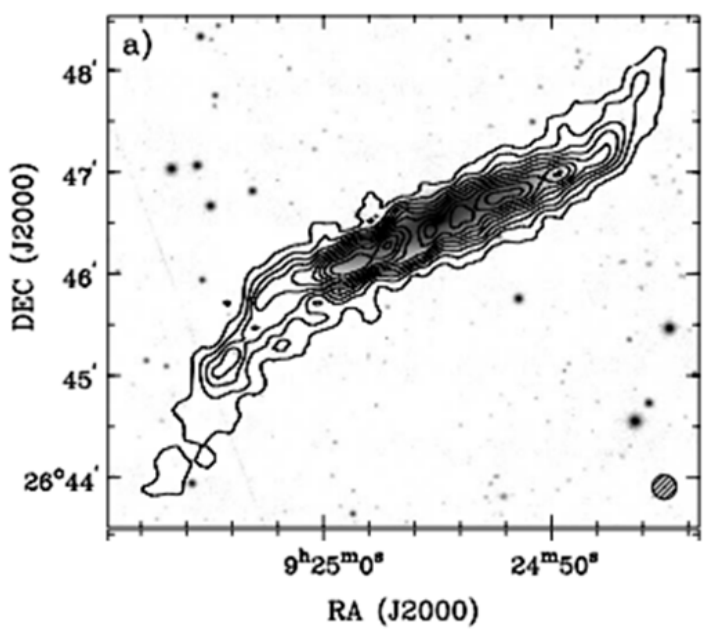

Figure 2.1: HI intensity contour plot of NGC 2862 overplotted on an I-band image. An HI warp can be seen as the change in orientation with respect to the inner disk of the contour lines on the outskirts of the galaxy. The intensity contours are uniformly weighted and range from 1.3×10^{20} to $3.8 \times 10^{21}\,\mathrm{cm}^{-2}$ in $3.2 \times 10^{20}\,\mathrm{cm}^{-2}$ intervals. Image credit: Spekkens and Giovanelli (2006).

to the optical disk, it has an HI warp. This extremely high rate of occurrence suggests that warps are either stable over long periods or continuously being excited. This may be the case, however the origin and sustainment mechanisms for warps are still under debate.

2.2.2 Warp Radius and Warp Strength

As mentioned in section 1.1, galactic warps can be seen as luminous material inclined with respect to the plane of the flat part of the disk. The Milky Way contains a warp in both its HI disk (Levine et al., 2006) and its stellar disk (Skowron et al., 2019). Figure 2.2 shows the stellar warp present in the Milky Way as measured using Cepheid stars. One can imagine this galaxy as containing two disks: a flat inner disk and a warped outer disk. As such, we can define the warp radius (r_w) as the distance from the center of the galaxy to the point where we transition from the flat inner disk to the warped outer disk. Warped galaxies can take a variety of shapes. For example, some

galaxies have warps only on one side; others have asymmetric warps where one side of the galaxy is more strongly warped than the other. In this thesis, we will only analyse warps that have the same strength and same r_w on either side of the center of the galaxy (idealised symmetric warps).

The strength of a warp away from the disk plane in an edge-on system can be defined in several different ways. One common way is by defining the alpha (α) angle. α is the angle between the center of the galaxy and the outermost isophote. The larger this angle, the further the warp has deviated from the inner ring. To better define a warp, some authors also use the beta (β) angle (Ann and Park, 2006; Sánchez-Saavedra et al., 2003). β is the angle from r_w to the tip of the outermost isophote. The β angle complements the commonly used α angle in that it allows us to differentiate between a weak warp that extends far out and a short, but steep warp. A visual depiction of α and β is shown in Figure 2.3.

Several studies were performed on populations of edge-on galaxies in order to determine the range of warp angles exhibited by nearby galaxies. From a sample of 325 edge-on galaxies ($i \geq 84°$) Ann and Park (2006) found warp angles varying from $1° < \alpha < 16°$ and $4° < \beta < 26°$. In their study, García-Ruiz et al. (2002) found warp angles between $0.7° < \alpha < 32.8°$, while Sánchez-Saavedra et al. (2003) found warp angles varying from $0° < \alpha < 25°$ and $0° < \beta < 45°$. Furthermore it has been found that there is no correlation between galaxy morphology, such as the incidence of bars or tightness of spiral arms, and warp frequency or warp strength (Ann and Park, 2006; Sanchez-Saavedra et al., 1990; Sánchez-Saavedra et al., 2003; Reshetnikov and Combes, 1999).

2.2.3 Theories on the Origin of Warps

One of the older theories on the origin of warps is that of intergalactic accretion (Kahn and Woltjer, 1959). In this theory, intergalactic matter, such as gas, is continuously accreted to the host galaxy but with a different net angular momentum. The more massive inner portion of the galaxy reorients the accreted material, and hence is able to maintain its orientation. On the other hand, the less dense outer portion of the disk is tilted due to its interaction with the infall material (Ostriker and Binney, 1989).

A second theory is that of misalignment between the galaxy disk and dark matter halo. In this theory gas is once again accreted with a different angular momentum, which reorients the angular momentum of the dark matter halo once every Hubble time. The disk will then reorient itself to align with the halo, but the alignment will not happen at the same time for all radii: the inner (more massive) parts re-align faster, creating an S-shape warped disk

(Ostriker and Binney, 1989; Binney, 1992; Ruiz, 2001).

A third theory is that of tidal interactions. This theory states that warps originate from the gravitational interaction between two neighbouring galaxies. García-Ruiz et al. (2002) have shown that most large asymmetric warps have tidal origins. Furthermore, in a study of optical warps, Reshetnikov and Combes (1998) found that the fraction of warped galaxies and their amplitudes were larger when in rich environments.

A fourth theory is that of intergalactic magnetic fields. Battaner et al. (1990) demonstrated that a magnetic field could cause warps in galaxies. In this theory, the magnetic field changes the orientation of the hydrogen gas, but not that of the stars. As such, the hydrogen gas would be strongly warped; young stars born from this gas would be mildly warped; and older stars would have very little to no warp (Battaner et al., 1990; Ruiz, 2001).

The final theory we will discuss is the discrete normal modes theory. Binney (1992) explains that the basic principle of this theory is that HI gas clouds move approximately in a circular orbit. If a cloud's orbit is inclined with respect to the galaxy plane, its height above this plane will oscillate harmonically at angular frequency $\nu = \sqrt{\delta^2\Phi/\delta z^2}$, where Φ is the galactic potential and z is the height above the galaxy plane. Meanwhile the cloud's azimuthal coordinate circulates with angular frequency $\Omega = R^{-1/2}(\delta\Phi/\delta R)^{1/2}$. Where R is the cloud radius. The angle at which the cloud crosses the equatorial plane will precess as $\omega_r = \nu - \Omega$. This means that the line of nodes of this gas cloud will change at each period of rotation, in a way that causes it to wind up like a spiral arm. This is the phenomenon observed by Briggs (1990). This theory becomes far more complex when more components and interactions within the galaxy are considered.

So far, none of these theories have been able to explain the origin of warps fully and many are still being improved. Elucidating the origin of warps is however not our objective. Rather we are interested in their effects on kinematic models.

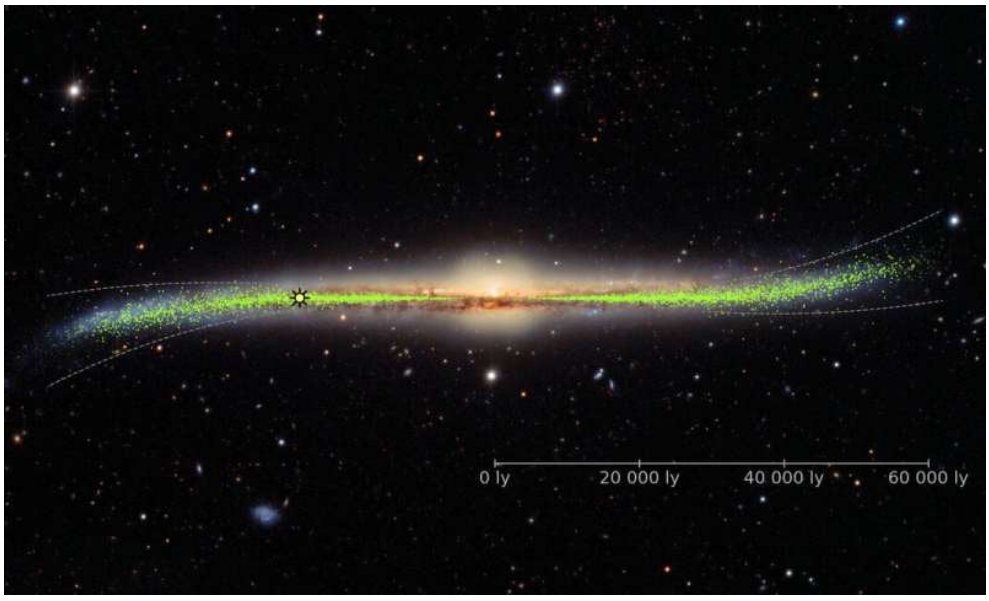

Figure 2.2: Model projection of observed Cepheid stars (green dots) overplotted on an artist's rendition of the Milky Way. The presence of a warp can clearly be seen. Image Credit: J. Skowron / OGLE / Astronomical Observatory, University of Warsaw.

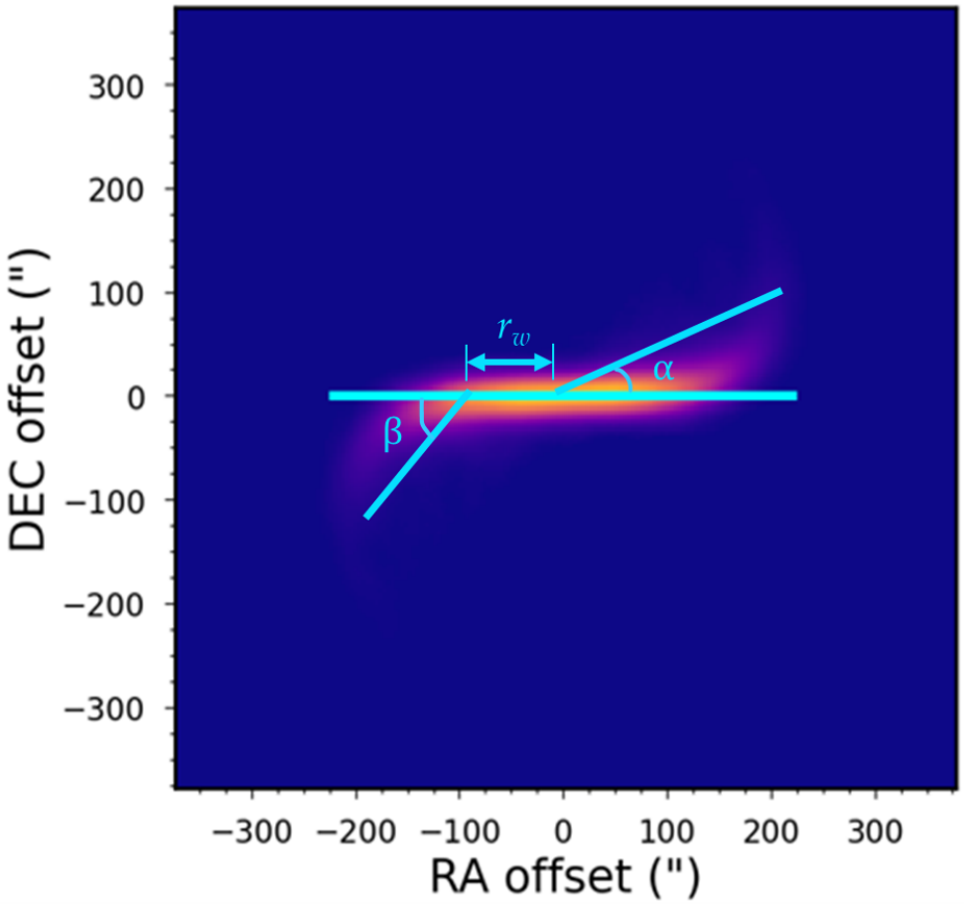

Figure 2.3: False-colour image of the HI gas distribution in a mock edge-on galaxy superimposed by a diagram showing r_w, α and β. The HI gas distribution was generated with MCG (Deg and Spekkens, 2023a).

2.3 Tilted Ring Modelling

In astronomy, kinematic modelling is the process of creating a model that describes the geometric parameters and motion of a galaxy. For disk galaxies, this includes but is not limited to a galaxy's inclination, position angle, systemic velocity and rotation curve.

Tilted ring models are a type of kinematic model used to describe the radial structure of galaxy disks. The first tilted ring model was created by Rogstad et al. (1974). Since particles rotate nearly circularly in a disk galaxy, the authors represented them by a set of concentric rings, of increasing radius. Each ring was given a rotational velocity, an inclination and a position angle. Figure 2.4 depicts the mean velocity field of M83 and the tilted ring model created from this velocity field.

Over the years, the original tilted ring model was modified, with various objectives in mind. For example, there is the ROTCUR function of the GIPSY software (Van der Hulst et al., 1992); KINEMETRY (Krajnovic et al., 2006) that is used for integral field unit observations of elliptical galaxies at optical wavelengths; DISKFIT (Spekkens and Sellwood, 2007), which is used to determine the velocity of non-circular motion in galaxies; and 2DBAT, which implements Bayesian fits of 2D tilted-ring models in order to derive rotation curves of galaxies (Oh et al., 2018).

Tilted ring algorithms as those mentioned above rely on finding the solution to the function:

$$V(x, y) = V_{sys} + V_{rot}(r)\cos(\theta)\sin(i) \tag{2.1}$$

with

$$\cos(\theta) = \frac{-(x - x_{pos})\sin\phi + (y - y_{pos})\cos(\phi)}{r} \tag{2.2}$$

$V(x, y)$ is the line of sight velocity as position (x, y) in the sky, V_{sys} is the galaxy's systemic velocity, V_{rot} is the rotational velocity and i is the galaxy's inclination. ϕ denotes the position angle, and x_{pos} and y_{pos} denote the center of rotation (Begeman, 1987). Each ring can then be specified by the parameters V_{sys}, V_{rot}, i, ϕ, x_{pos} and y_{pos}. Note the direct relation between $V(x, y)$ and $\sin(i)$.

Each of these algorithms is effective at solving the specific questions it was meant to answer. They also all create their model by fitting the rings to a velocity field (a 2D representation of the gas motion), created from HI line emission observations. This can lead to two problems. First, the velocity field does not constrain the model enough, therefore the fitting process must involve human interactions (Kamphuis et al., 2015). Second, the velocity field may not contain all the available information: after all, it is a 2D moment of the

3D data cube in the frequency/velocity dimension. In particular, the velocity field is constructed from HI line emissions, which come in the form of data cubes. These data cubes have three dimensions. Therefore, in order to obtain a velocity field, the data cube must be compressed. This compression causes a loss of information. Most importantly, it causes beam smearing, especially for galaxies with resolutions below 7 - 8 beams across the HI disk (Bosma, 1978; Kamphuis et al., 2015; Lewis, 2019). This is an issue for WALLABY as most detections will be at or below this resolution. Furthermore, the non-circular motion of gas can affect the accuracy of the velocity field (de Blok et al., 2008).

These issues can be avoided by fitting the tilted ring model directly to the 3D data cube. Several kinematic modelling tools do exactly that. The three most popular are: the Tilted Ring Fitting Code[1] (TiRiFiC, Jozsa et al. 2007), 3DBAROLO[2] (Teodoro and Fraternali, 2015), and the Fully Automated TiRiFiC[3] (FAT, Kamphuis et al. 2015). FAT is not a standalone programme, but rather a wrapper around TiRiFiC and the Source Finding Application (SOFIA, Serra et al. 2015), which enables fully automated tilted-ring fits, by iteratively applying TiRiFiC.

Since many WALLABY galaxies will be marginally spatially resolved, this thesis tests the performance of a 3D code on low resolution mock galaxies. Furthermore, the hundreds of thousands of anticipated detections make a fully automatic modelling tool a necessity. TiRiFiC does its optimization fully in 3D, whereas 3DBAROLO does some steps in 2D. This makes TiRiFiC, as automated by FAT, the best choice for this project.

[1] https://gigjozsa.github.io/tirific/
[2] https://editeodoro.github.io/Bbarolo/
[3] https://github.com/PeterKamphuis/FAT

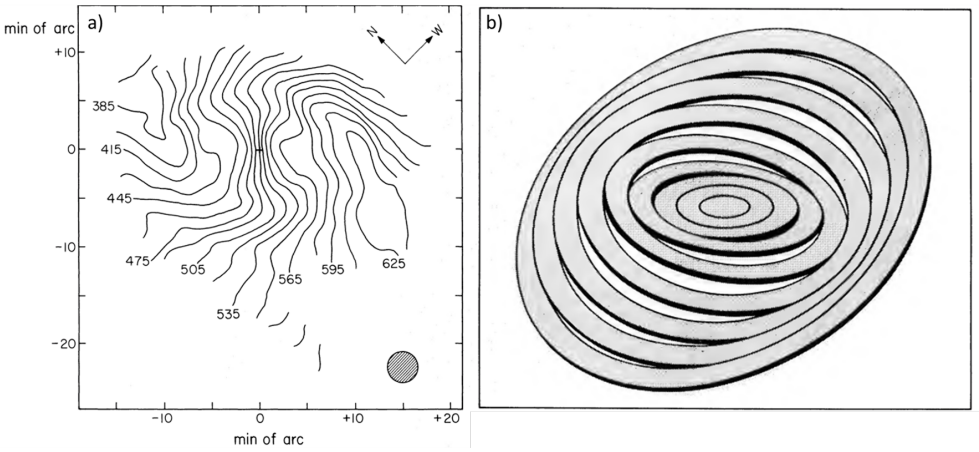

Figure 2.4: Weighted mean velocity field of HI in M83 (panel a) and the tilted-ring model created from this velocity field (panel b) as viewed 90° for the line of sight, so the observer is in the plane of the paper at the top of the page. Image credit: Rogstad et al. (1974).

2.4 FAT

In this section, we will have a brief look at how FAT performs it fitting process. For more details on the subject see Kamphuis et al. (2015). FAT was designed to fit a model to a 3D data cube without the need for user input initial estimates nor the need for a user to tweak any parameters to obtain the final result. It does not use all of TiRiFiC's flexibility, but can fit both asymmetric disks and warped disks. This version of the code is also a prototype for the 3D branch of the WALLABY kinematic pipeline and the WALLABY Kinematic Analysis Proto-Pipeline (WKAPP, Kamphuis et al. 2015; Deg et al. 2022).

2.4.1 FAT Inputs

FAT requires an input catalogue, a configuration file and a source cube. The input catalogue lists all the galaxies that one wishes to run through FAT; the configuration file controls how the fitting process will occur; and the source cube is the data cube for the galaxy in Flexible Image Transport System (FITS) file format[4]. The catalogue and source cube are self explanatory and do not require further explanation, however we will discuss certain parameters of the configuration file.

As seen in Figure 2.5, there are 16 parameters to enter in the file; we will

[4]https://fits.gsfc.nasa.gov/fits_standard.html, accessed on 27-04-2023

cover the function of several of them here. “startgalaxy” and “endgalaxy” simply refer to the identification number of a galaxy in the catalogue. The “allnew” line indicates the type of input for the initial estimates. Throughout this thesis, no pre-processing was done and this line was kept at a value of -1, meaning that FAT determined the initial estimates from the input data cube. The “finishafter” line indicates when FAT will stop the fitting process; if set to 1 the fit finishes early, by stopping after the initial flat disk is fit. If set to 2, a second fit is done to optimize the parameters. Throughout this thesis this parameter was set to 2. “catalogue” and “maindir” are the paths to your catalogue and directory containing the observational data. “opt_pixelbeam” refers to the number of pixels per beam. If “warp_output” is set to 1, FAT will provide a tiltogram, warp radius (r_w) and maximum angles of the fitted warp. The tiltogram is a diagram of the inclination of the disk at one radius with respect to the disk at another radius. The “fix_incl”, “fix_pa” and “fix_sdis” determine whether FAT will allow the inclination, position angle and surface brightness distribution to vary with radius. If set to 0, these values will be the same for all rings in the model; if set to 1 each ring can have a different inclination, position angle and/or surface brightness distribution respectively.

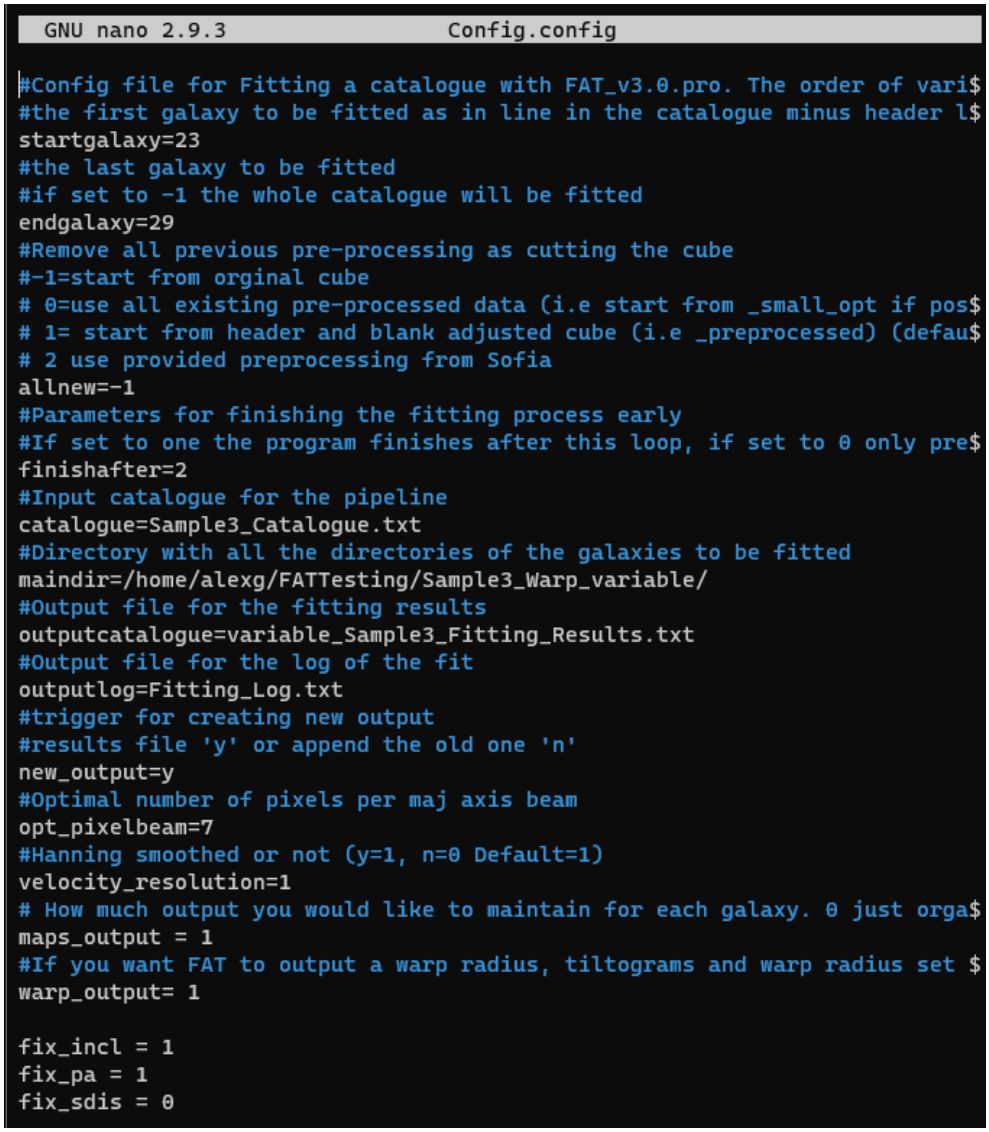

Figure 2.5: Example of a configuration file required by FAT.

2.4.2 FAT Fitting Process

Prior to beginning its fitting process, TiRiFiC requires initial estimates. FAT obtains the estimates of the velocity width, galaxy size and galaxy centre via SOFIA (Serra et al., 2015). Furthermore, it uses the moment maps created from SOFIA's mask to determine initial estimates for inclination and position angle. With these estimates in hand, FAT runs the first iteration of TiRiFiC on the data cube.

In its first fitting loop, FAT fits a flat disk model. Only the surface brightness and rotational velocity vary from ring to ring; all other parameters are kept fixed. The objective of this step is to accurately determine the center of the galaxy, while keeping the other parameters within the initial estimates. If a central location is not found within 50 iterations of TiRiFiC, or if the other parameters fall outside the estimated boundaries, the fitting process is halted and flagged as a fail. This is also referred to as a model failing to converge to a solution.

If the flat disk model is successful, FAT runs a second fitting process. In this iteration, the inclination and position angle are allowed to vary radially if FAT's estimate of $N_{beam} \geq 6$ (FAT's estimate of N_{beam} corresponds to the number of beams that fit in the FAT estimated D_{HI}). For FAT estimates of $N_{beam} < 6$, inclination and position angle are kept fixed from ring to ring. Additionally, the galaxy is split along the minor axis and both sides are fit independently. The model is then optimized in 3D (one spectral channel at a time) using an implementation of the 'golden section' search algorithm (Press et al., 1992). When the model is accepted, the radial variation of the parameters is smoothed by a polynomial of order 0, 2, 3, 4 or 5 to avoid artificial fluctuations from the TIRIFIC fitting algorithm. The difference between the smoothed and unsmoothed curves is returned as uncertainties.

2.4.3 FAT Outputs

If the fitting process is successful, FAT outputs a final model in the form of a FITS file accompanied by a data file containing the estimated parameters and uncertainties. Additional files are also output, such as a fitting log, which explains what has happened at each step of the process, the moment maps created with SOFIA, a position-velocity diagram, information pertaining to the warp (if this option was selected in the configuration file) and several others.

2.4.4 FAT Performance

An in-depth analysis of FAT's ability to recover warped galaxy morphology has not been done before and will be the subject of Chapter 4. However, three analyses of FAT's performance were completed to date (Kamphuis et al., 2015; Lewis, 2019; Deg et al., 2022).

In their analysis, Kamphuis et al. (2015) used two samples of galaxies. The first was a set of 52 mock observations built around two base rotation curves: the first being slow rising, typical for an intermediate mass galaxy; the second being based on a smoothed version of the rotation curve of NGC 891 (Oosterloo et al., 2007; Fraternali et al., 2011) to represent massive galaxies. In order to create base models resembling the aforementioned rotation curve, Kamphuis et al. (2015) adopt an exponential surface brightness profile with a truncation at a specific radius. Other parameters were set to optimize tilted ring fitting.

The authors then varied one parameter at a time to generate 25 intermediate mass models, 25 high mass models and 2 dwarf galaxies. The sample of mock galaxies led Kamphuis et al. (2015) to conservatively conclude that FAT can accurately recover the kinematics and morphology of galaxies with $N_{beam} \geq 8$ and $20^\circ \leq i \leq 90^\circ$(Kamphuis et al., 2015).

The second set was comprised of 25 galaxies taken from the Local Volume HI Survey (LVHIS, Koribalski 2010) catalogue, which allowed the fitting code to be tested on real data. FAT successfully modelled 23/25 of these galaxies in the sense that the data cube HI emissions were accurately traced by the model.

Lewis (2019)'s analysis focused on determining FAT's ability to model marginally resolved, flat disk galaxies, expected to be observed by the WALLABY survey. In order to do so, marginally resolved idealised mock galaxies for which the true tilted-ring parameters are known are generated, and then fed into FAT. The output values are then compared to the true values to determine the regime in which FAT is reliable. For this test, the idealised mock galaxies had input values of $10^\circ \leq i \leq 80^\circ$, $7.0 \leq M_{HI} \leq 9.0\, dex\, M/M_\odot$ and $1.5 \leq N_{beam} \leq 7.0$ (see Table 5.1 of Lewis 2019).

50 different noise realisations were then added to each mock data cube. FAT was run on each resulting mock datacube. The median of the 50 modelled rotation curves (for 1 underlying model) is then compared to the input model's rotation curve. In this paper, several different success criteria were evaluated, however, they all indicate a similar trend in terms of FAT's limitations. The author concludes that the disk geometry and rotation curve can be accurately recovered for galaxies with $35^\circ < i < 80^\circ$ if a) $N_{beam} \geq 4$ and $V_{rot}(R_{HI}) < 25\,\mathrm{km\,s^{-1}}$; or b) $N_{beam} \geq 3.5$ and $V_{rot}(R_{HI}) > 25\,\mathrm{km\,s^{-1}}$ (Lewis, 2019).

FAT has continued undergoing development over the past years and there-

fore may perform better than stated here. As such, we have analysed FAT's performance in a similar manner as Lewis (2019) and will compare our results to his. This will be presented in Chapter 3.

2.5 MCG

The data cubes, in the form of Flexible Image Transport System (FITS) files, required as inputs for FAT were created using the Mock Cube Generator (MCG, Deg and Spekkens 2023a). MCG is a standalone data cube generator, that uses scaling relations to produce realistic mock observations. Using MCG over FAT's intrinsic ability to generate data cubes has the advantage that two completely independent programs are used. The scaling relations used can be found in (Deg and Spekkens, 2023b), while the detailed process of how the cubes are generated can be found in (Deg and Spekkens, 2023a).

We will however describe the basic steps MCG uses to generate its mock observations. Figure 2.6 shows a visual representation of these steps. First, the user inputs the galaxy's M_{HI}. From this MCG uses the HI mass-diameter relation of Wang et al. (2016) to determine its diameter and maximal rotational velocity. Based on the observed size, the distance is determined, in such a way to get the user specified N_{beam}. From this a set of nested rings is defined (step 1 in Figure 2.6). Each ring is then filled with tracer particles, which are given a rotational velocity (step 2 in Figure 2.6). Then, using user input observational parameters (inclination, position angle and galaxy center coordinates) the particles are projected in sky plane (step 3 in Figure 2.6). During this projection radial velocities are determined. These velocities are depicted in red and blue for receding and approaching (respective to the systemic velocity) line of sight velocities, respectively. Each particle is then placed in a spatial and spectral cell of the mock data cube. To make the observation realistic, the source cube is convolved spatially and spectrally to a user-specified resolution, then Gaussian random noise is added.

The mock data cube has three axes: two spatial axes and one spectral axis. The user inputs the wanted pixel and channel units. Spatial units can either be in degrees or arcseconds, spectral units can be in either $\mathrm{km\,s^{-1}}$ or in $\mathrm{m\,s^{-1}}$. The user may also specify the pixel dimensions and channel size. In this thesis, the spatial axes were set in arcseconds, with each pixel representing 6". Each channel (width of the spectral pixel) represented 4 $\mathrm{kms^{-1}}$, in order to mimic WALLABY observations. Once the data cube is populated with the mock galaxy, each pixel is given a spectral brightness in units of Jansky per beam ($\mathrm{Jy\,beam^{-1}}$), where $1\,\mathrm{Jy} = 10^{-26}\,\mathrm{W\,m^{-2}\,Hz^{-1}}$.

Two programmes of the MCG suite can be used to generate mock observa-

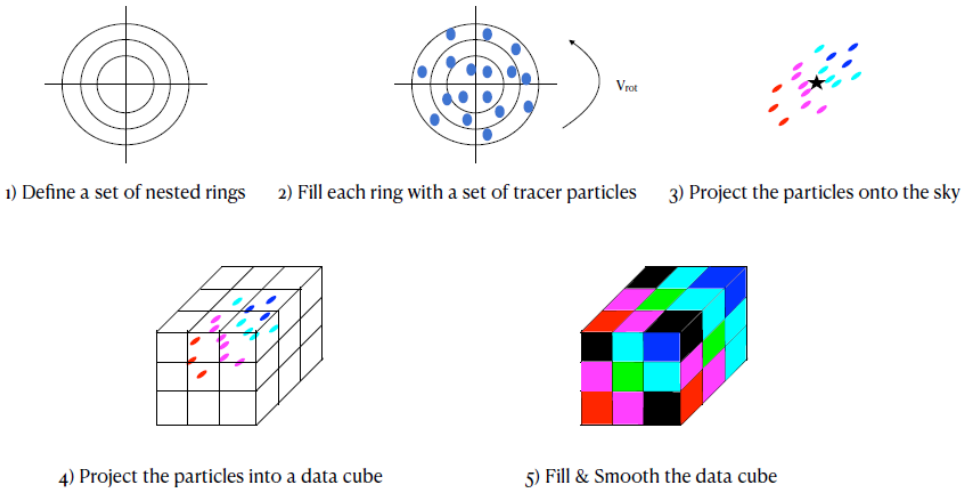

Figure 2.6: Process showing how MCG creates its mock data cubes. Image credit: Deg and Spekkens (2023a)

tions: the *make_galaxy* and *make_suite* programmes. *Make_galaxy* uses the above process to generate a single mock HI observation with the user specified parameters. *make_suite* is used to generate a number of mock observations in a single run of the programme. The user specifies all the parametric combinations for which mock observations are wanted and specifies the number of noise realizations for each mock observation. In this thesis, the *make_suite* functionality was used.

2.6 This Thesis

In this thesis, we will generate data cubes containing mock galaxies using the MCG. These data cubes will then be put through FAT. The resulting model will be compared to the original galaxy in order to answer the four following questions:

1. To what limits can FAT accurately model a galaxy's rotation curve?
2. Do these limits change when the galaxies contain a warp?
3. Under which conditions can FAT identify the presence of the warp?
4. Can the rotation curves of warped galaxies be approximated by flat disk models?

This last question is of particular interest because it may save researchers several hundred computational hours. Surveys like WALLABY and those of the future SKA will detect hundreds of thousands of galaxies, many of which will be warped. If the rotation curve of warped galaxies can indeed be approximated by a flat disk model, there is no need to perform the additional steps required to parameterize the warp. These steps require additional computation time. Even if this additional time is small for a given galaxy, the total additional computational time is very large, due to the sheer number of galaxies that need to be analysed.

The remainder of this thesis is separated as follows. In Chapter 3, we will generate flat models of flat galaxies, in order to answer question 1. In Chapter 4 we will generate warped models of warped galaxies, in order to answer questions 2 and 3. We will then force FAT to generate flat models of warped galaxies and compare these results to those of Chapter 3, to answer question 4. Finally, in Chapter 5, we will provide closing remarks and discuss future work.

Chapter 3

FAT Models of Flat Disks

The Fully Automated TiRiFiC programme was created in 2015, and has undergone continuous improvements until late 2020. FAT has been tested under a number of conditions in the past (Kamphuis et al., 2015; Lewis, 2019), however these tests were done prior to the latest release. In this Chapter, we will determine FAT's ability to recover the rotation curve of marginally resolved flat (unwarped) disk galaxies using the latest version (V2.0.1) and compare our results with those of previous studies. We will do so with two different tests. In section 3.1, we use a statistical analysis to determine which parametric combinations result in a successful fits; while in section 3.2, we generate a realistic set of observations to narrow down the parametric combinations that result in a successful fit.

3.1 Benchmarking FAT

3.1.1 Methodology

Mock Dataset Generation

A set of base models was created by inputting a range of M_{HI}, i, and N_{beam} in MCG's *Make_Suite* program. The PA and velocity dispersion are held fixed because the absolute value of the PA does not impact the fitting (unlike the inclination, which does), and the input value and fitted value of the velocity dispersion don't affect the recovered rotation curve (Deg et al., 2022). The PA was set to 45° and the velocity dispersion was set to 10 $\mathrm{km\,s^{-1}}$. The root mean square (rms) noise was set to 1.6 $\mathrm{mJy\,beam^{-1}}$, to mimic WALLABY-like values Koribalski et al. (2020). The list of values used is presented in Table 3.1. The models were generated by varying one parameter at a time, creating a total of 72 base models. 50 unique noise realizations were then added to

Table 3.1: List of parameters used to create the 72 base models. Each parametric combination was used to create one mock HI observation.

Parameter	Values	Units
M_{HI}	7.5; 8.3; 9.2	$\log(M_{HI}/M_{\odot})$
i	10; 35; 65; 80	degrees
N_{beam}	2.5; 3.0; 3.5; 4.0; 4.5; 5.0	Beams across major axis

each base model, generating a total of 3,600 models. Each model was then independently analyzed by FAT. The data output by FAT was used to generate two separate rotation curves for each model. The first is the rotation curve as calculated by FAT; the second is an inclination corrected rotation curve.

The FAT recovered rotation curve is simply the result obtained by running each realization through the FAT fitting process without priors and in "flat fitting mode". The inclination corrected rotation curve is determined because when FAT's estimate of the inclination is wrong, the recovered rotation curve is strongly affected (Lewis, 2019). Thus calculating the inclination corrected rotation curve allows us to assess FAT's performance in the case where the inclination is known from observational methods. Equation 2.1 shows that the recovered velocity directly relates to $\sin(i)$. As such, the inclination corrected rotation curve was determined using:

$$\mathrm{FAT_{Vrot,corr}(r)} = \mathrm{FAT_{Vrot}(r)} \frac{\sin(\mathrm{i_{FAT}})}{\sin(\mathrm{i_{MCG}})} \tag{3.1}$$

where $\mathrm{FAT_{Vrot,corr}}$ is the rotational velocity after inclination correction; $\mathrm{FAT_{Vrot}}$ is the rotational velocity as calculated by FAT; i_{FAT} is the inclination as estimated by FAT; and i_{MCG} is the model's true inclination.

Evaluation Criteria

In order to determine whether or not a FAT model successfully recovered the rotation curve, only data points within 15" $< r \leq R_{HI}$ were considered. Data points within a radius of half a beam FWHM from the galaxy center were not considered as FAT has a known issue of overestimating at these radii (Kamphuis et al., 2015). Data points at $r > R_{HI}$ were also not considered as the surface brightness is low in this region and observational noise can have large impacts on results. The acceptable deviation from the input value was set to 15% of the input rotational velocity at R_{HI}. For example if MCG's $V_{rot}(R_{HI}) = 100\,\mathrm{km\,s^{-1}}$, the acceptable deviation in $V_{rot}(r) = 15\,\mathrm{km\,s^{-1}}$. This value was chosen so the error margin would scale with absolute value. This does however come with the consequence of favoring more massive galaxies

as their rotational velocities are larger. These radial and rotational velocity limits create an "Acceptable fit zone". This zone is represented by the light red box in the right hand plots of Figure 3.1.

Figure 3.1 shows a visual representation of the evaluation criteria. The top row shows the rotation curve (left) and residuals (right) as evaluated by FAT. The bottom row shows the rotation curve (left) and residuals (right) after inclination correction (Equation 3.1). Blue crosses represent the model recovered rotation curve, blue dots represent the residuals between the model and input, and red lines are the input values. Note that each diagnostic plot contains the data from 50 models: 50 noise realizations of 1 underlying model, but that the number of data points varies based on the number of converging models. As such, the rotation curve of an individual realization can be represented by a line connecting one cross (left panel) or dot (right panel) at each radius at which the model is evaluated. The blue horizontal lines are the medians for each radial bin.

Given the definition of the acceptable zone, two separate analyses were performed. In the first analysis, individual rotation curves were assessed. This method will henceforth be referred to as the *by curve* analysis. In this analysis, if all data points for a given curve were within the acceptable fit zone, the FAT fit was deemed a success. If one or more data points for that curve were outside the acceptable fit zone, or if the fit of the realization failed to converge, the FAT fit was deemed a failure. The total number of successes were added for each base model and converted to a percentage. Results can be found in Figure 3.2.

In the second analysis, the FAT recovered values of the rotation curve were grouped in radial bins. The median V_{rot} of each bin was then computed and compared to the true value at a radius corresponding to the center of that bin. This method will henceforth be referred to as the *bin median* analysis. The bin width was set to 15", which corresponds to 1/2 the beam FWHM of the WALLABY survey. The galaxy was considered successfully modelled if the median of each radial bin lied within the acceptable fit zone and if a minimum of 75% of realizations converged. Results for this analysis can be found in Figure 3.3. The convergence rate for each set of mock realizations is presented in Figure 3.4.

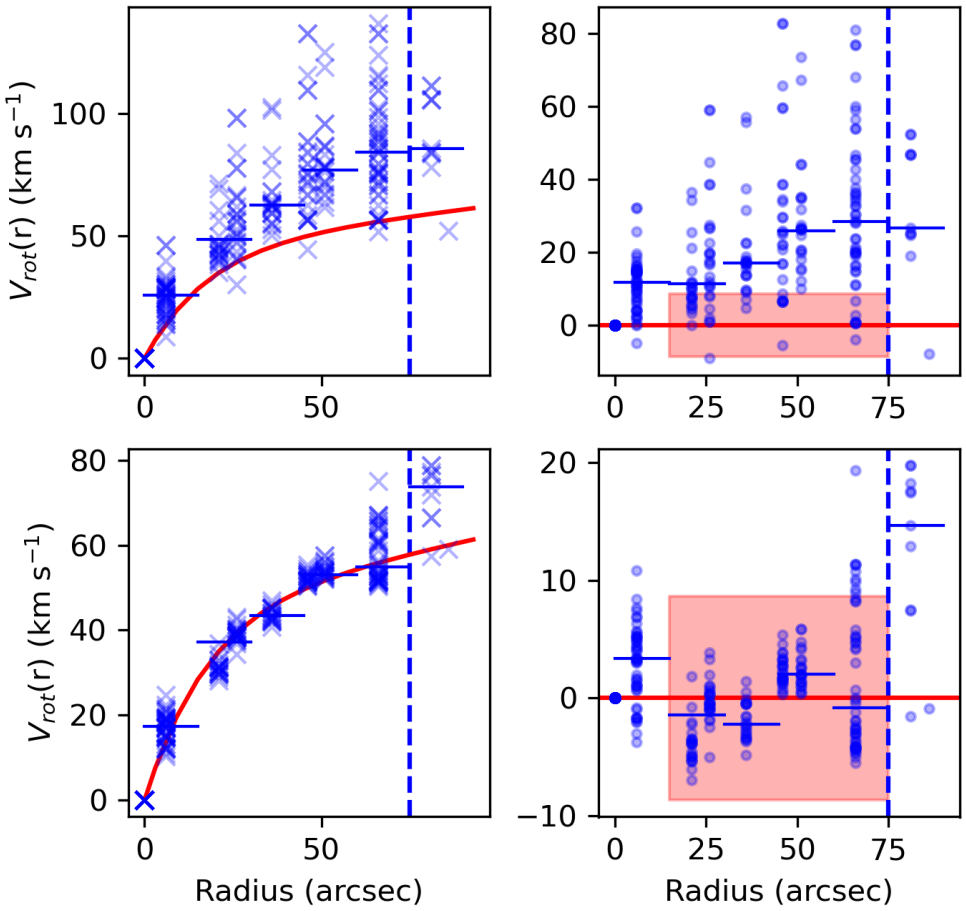

Figure 3.1: Diagnostic plot for all realizations of base model "ba_5.0.mass_8.3.inc_35.0.pa_45.0.veldisp_10.0". The left column shows the rotation curves as calculated by FAT (top) and after inclination correction (bottom). The right column shows the residuals of the corresponding rotation curve. The red line indicates the input value. Each blue cross in the left column represents a FAT calculated $V_{rot}(r)$. Each blue dot in the right column represents the residual between FAT and MCG. The vertical dashed blue line indicates R_{HI} and the horizontal blue lines show the median FAT recovered value for each radial bin.

3.1.2 Results

Rotation Curve Recovery by FAT

First we will analyze FAT's performance without the inclination correction. In this test, the results from both evaluation methods gave very similar results, with the *by curve* analysis being slightly more stringent. As can be seen in Figures 3.2 and 3.3, it is clear that galaxies with larger HI masses and higher inclinations are easier to fit. At $\log(M_{HI}/M_{\odot}) = 7.5$, FAT is unable to accurately recover the rotation curve regardless of the inclination. The few exceptions to this statement occur at $N_{beam} = 4$ with $i = 65°$ and $i = 80°$ in the *by curve* analysis, and at $N_{beam} = 4$ with $i = 65°$ with $i = 80°$ and at $N_{beam} = 3.5$ with $i = 80°$ in the *bin median* analysis. Note that at this time we had not yet evaluated at $N_{beam} = 8$.

It is strange that the success rate drops from 84% and 86% to 2% and 4% respectively when going from $N_{beam} = 4.0$ to $N_{beam} = 4.5$ in the *by Curve* analysis of $M_{HI} = 7.5\,\mathrm{dex}\,M/M_{\odot}$ (Figure 3.2). A similar effect can be seen in the *bin median* analysis (Figure 3.3). There is no obvious reason for this behaviour. It may be that the way FAT makes its initial estimates simply coincides nicely with the rotation curve shape and values in this regime. Ignoring these outliers, the data clearly indicates FAT's inability to properly recover the rotation curve at $M_{HI} = 7.5\,\mathrm{dex}\,M/M_{\odot}$ in the resolution regime tested.

In order to determine whether an increased spatial resolution would allow for the accurate recovery of the rotation curve at $M_{HI} = 7.5\,\mathrm{dex}\,M/M_{\odot}$, we have added a suite of galaxies with $N_{beam} = 8.0$. Results were added to Figures 3.2 and 3.3. Results lead us to believe galaxies with $M_{HI} = 7.5\,\mathrm{dex}\,M/M_{\odot}$ can be recovered if their spatial resolution is high enough; however the few data points that indicate this do not make a strong argument. Additional models in this regime would be required to confirm this.

These results are somewhat in line with those of Kamphuis et al. (2015) and Lewis (2019). Unlike what they found, our results show FAT has difficulty recovering the rotation curve for galaxies with an inclination $i \leq 35°$. Kamphuis et al. (2015) determined an acceptable inclination range of $20° - 90°$, while Lewis (2019) determined inclinations $35° - 80°$ yielded acceptable results. On the other hand, our analysis indicates FAT's ability to recover rotation curves for resolutions of $N_{beam} \geq 2.5$ at $i \geq 65°$ if $M_{HI} \geq 8.3\,\mathrm{dex}\,M/M_{\odot}$. This shows acceptable fits for lower spatial resolutions than determined by Kamphuis et al. (2015) (8 beams across) and Lewis (2019) (3.5 beams across). One factor that may explain some of these differences is our choice of evaluation criteria. By using 15% of $V_{rot}(R_{HI})$ as the acceptable deviation from the input

$V_{rot}(r)$ value, higher HI mass galaxies are advantaged since they have larger rotational velocities. This would explain why our sample had difficulty at $\log(M_{HI}/M_{\odot}) = 7.5$, while Lewis (2019)'s didn't. It may also explain why we find lower resolutions to be acceptable.

Inclination Corrected Rotation Curves

Looking at the inclination corrected results (yellow squares in Figure 3.3 and the bottom row of Figure 3.2), we immediately notice significant improvements in FAT's ability to recover the rotation curve. Almost all models improve. In both figures, we see significant improvements at $M_{HI} = 7.5\,\mathrm{dex}\,M/M_{\odot}$, however, this is still not a regime in which FAT is obviously successful. For $M_{HI} = 8.3\,\mathrm{dex}\,M/M_{\odot}$ and $M_{HI} = 9.2\,\mathrm{dex}\,M/M_{\odot}$, results from both evaluation methods agree that models at $i = 35°$ now yield acceptable results. The *bin median* analysis even shows good performance at $i = 10°$ for an $M_{HI} = 9.2\,\mathrm{dex}\,M/M_{\odot}$. These results are less optimistic than those of Lewis (2019), which conclude that models with $i \geq 10°$, $N_{beam} \geq 3$ and $M_{HI} \geq 8.3\,\mathrm{dex}\,M/M_{\odot}$ are well recovered.

Determining Which Parameter Limits FAT's Ability to Recover the Rotation Curve

In order to determine which parameter limits FAT's ability to recover the rotation curve, we have calculated the median recovered residual for the inclination, position angle and central coordinates of the galaxy (V_{sys} (spectral center), and x,y coordinates (spatial center)) for all 88 models (76 original models + 12 models at $N_{beam} = 8$). Results are shown in Figure 3.5. In this plot, each dot represents one model (i.e. the difference between the median of the model's 50 realizations and the input value). Note that since we generate the residual by subtracting the input value from the recovered value (FAT - MCG), a positive value signifies an overestimation on FAT's part and a negative value signifies an underestimation.

As can be seen in the first row, a large concentration of the data is near $\Delta i = 0$, meaning the inclination was well recovered in most cases. However, inclination also shows the greatest variability when compared to the other parameters (up to $> 50°$). There is also a systematic underestimation at $i = 35°$. This is clear when looking at the second set of dots in the upper left panel of the plot.

The second row indicates that, on average, FAT's estimate of the position angle is much better than that of the inclination. The PA varies up to 7° as opposed to the 50° seen in inclination. However, for certain galaxies the two

parameters have similar residuals. It is also clear that the PA value is harder to estimate for low mass, low inclination galaxies.

The systemic velocity is extremely well recovered. All models were constrained within 1 $\mathrm{km\,s^{-1}}$, which corresponds to 1/4 of a resolution element (spectral channels are 4 $\mathrm{km\,s^{-1}}$). Similarly, the spatial center of the galaxy is also very well recovered, varying by only a couple percent of a beam, with a maximum variation of 5% of a beam (i.e. up to 0.75").

This confirms our previous suspicions that, in most cases, the inclination estimation has the greatest variability an thus the greatest effect on our ability to recover the rotation curve. There are however models for which the PA may have a similarly large impact. We will now further investigate the effects of an improper estimation of the inclination.

Investigating Conditions and Effects of a Misestimated Inclination

In order to further evaluate how the inclination affects FAT's ability to recover the rotation curve, Figure 3.6 was created. This figure shows a diagnostic plot comparing $\Delta \sin(i)$ as a function of input inclination, mass and N_{beam}. This plot shows the difference between the sine of the FAT recovered inclination and the sine of the input inclination ($\sin(i_{\mathrm{FAT}}) - \sin(i_{\mathrm{MCG}})$) because the model being optimized depends on V_{rot} and $\sin i$ (see equation 2.1).

We begin by discussing the three outliers (the three data points with $\Delta \sin(i) \sim -0.75$). Contrary to the rest of the data, these data points have a very large $\Delta \sin(i)$ despite having large initial inclinations. These galaxies also happen to have a low mass (7.5 dex) and a very low resolution ($N_{beam} = 2.5$ and $N_{beam} = 3$). We will not consider these three points for the rest of our analysis as this is a regime in which FAT has difficulty (See Figures 3.2 and 3.3.

The leftmost panel of Figure 3.6 shows that lower input inclination cause larger variations in the recovered $\Delta \sin(i)$. This is in part because the $\Delta \sin(i)$ will be accentuated at low inclinations (i.e. for the same Δi a low inclination galaxy will have a larger $\Delta \sin(i)$). The second panel indicates there is no clear correlation between $\Delta \sin(i)$ and input M_{HI} (which dictates the rotation curve shape), while in the third panel, we see a small decrease in $\Delta \sin(i)$ for galaxies with larger angular size. Overall, Figure 3.6 shows that when the input inclination is small, there is a larger chance of having a large $\Delta \sin(i)$, which will in turn cause a miscalculation of the rotation curve. Thus, low inclination galaxies have a higher probability of not being fit properly. Lower resolution galaxies follow the same phenomenon, but to a lesser extent. These results are perfectly in line with what we see in the evaluation of the rotation curve (Figures 3.2 and 3.3).

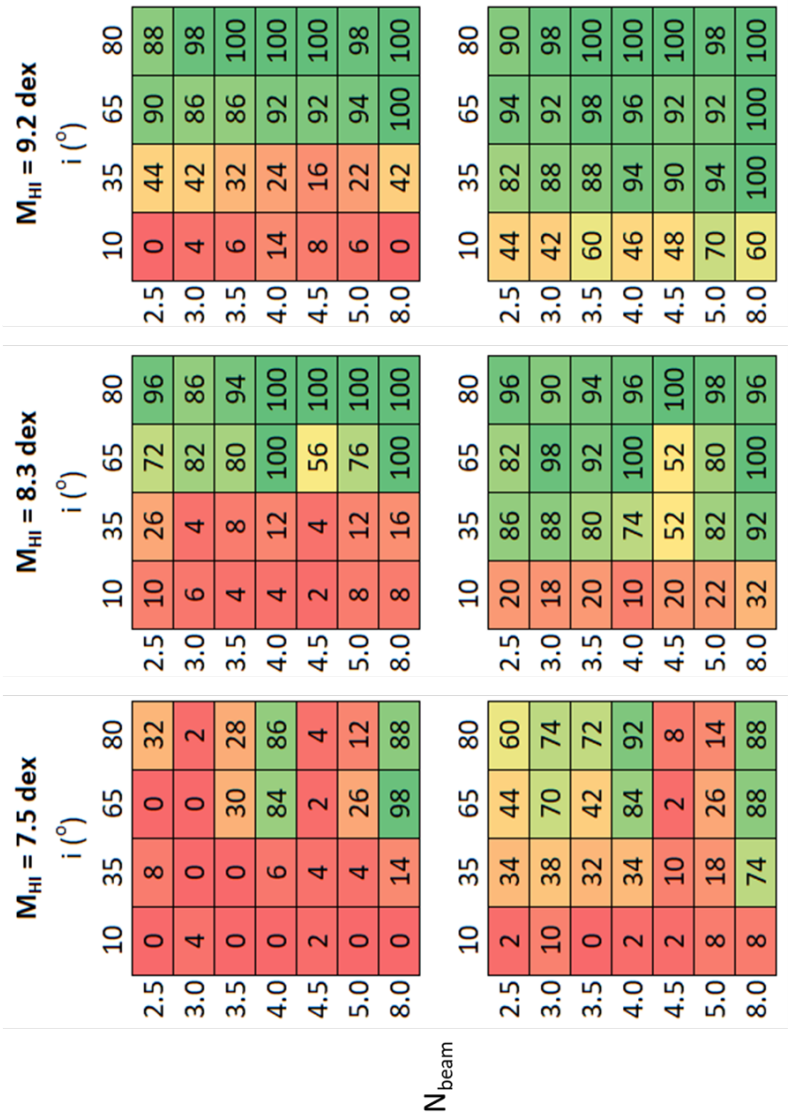

Figure 3.2: Results of the *by curve* analysis. Each box corresponds to a set of fits to 50 realizations of a mock galaxy with the HI mass given above the table, with N_{beam} specified by the row label and inclination specified by the column label. The number in each box represents the percentage of successfully recovered rotation curves for that base model. The top row shows the results as determined by FAT. The bottom row shows the results after inclination correction. The colour scheme goes from red (0%) to green (100%) success rate.

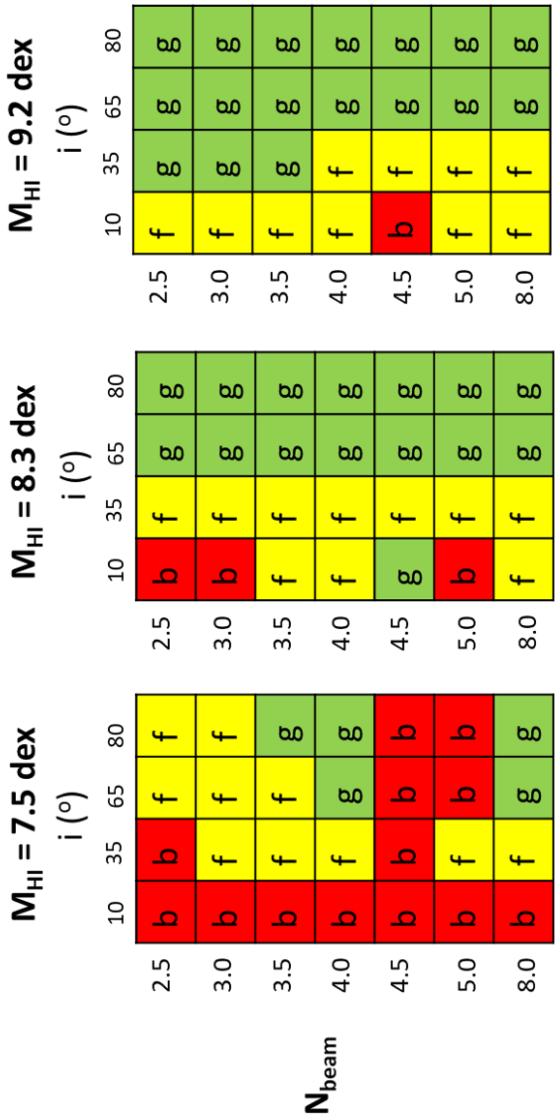

Figure 3.3: Results of the *bin median* analysis. Green boxes with the letter 'g' indicate that mock galaxies with the properties corresponding to that box are deemed to be reliably recovered by FAT; yellow boxes with the letter 'f' indicate mock galaxies with the properties corresponding to that box are deemed to be reliably recovered after inclination correction; and red boxes with the letter 'b' indicate failures even if the inclination is fixed to the true value.

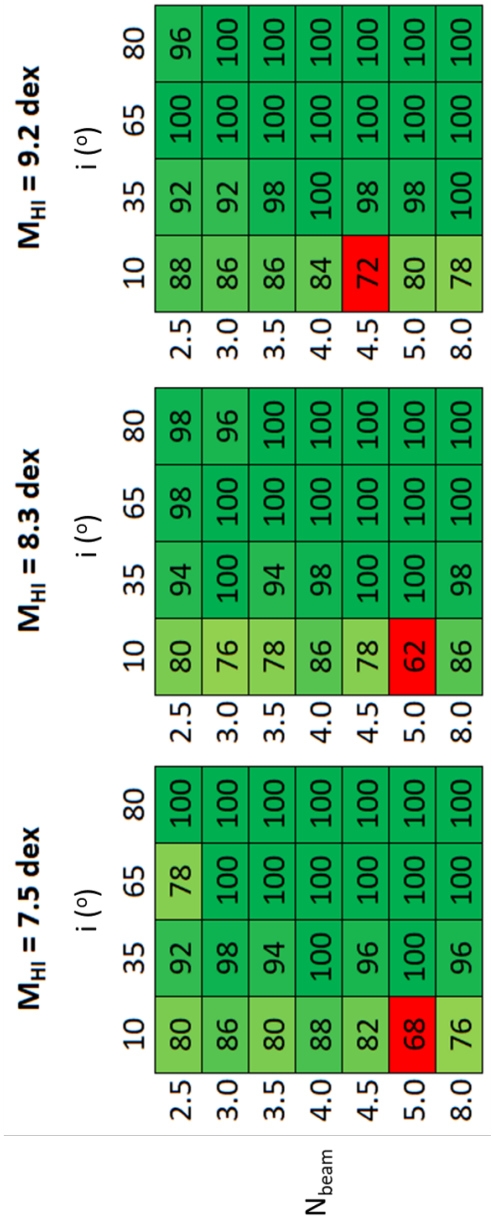

Figure 3.4: Percentage of converging realizations for each base model. Models for which $< 75\%$ of realizations converged are highlighted in red as they imply a failure in the *bin median* analysis.

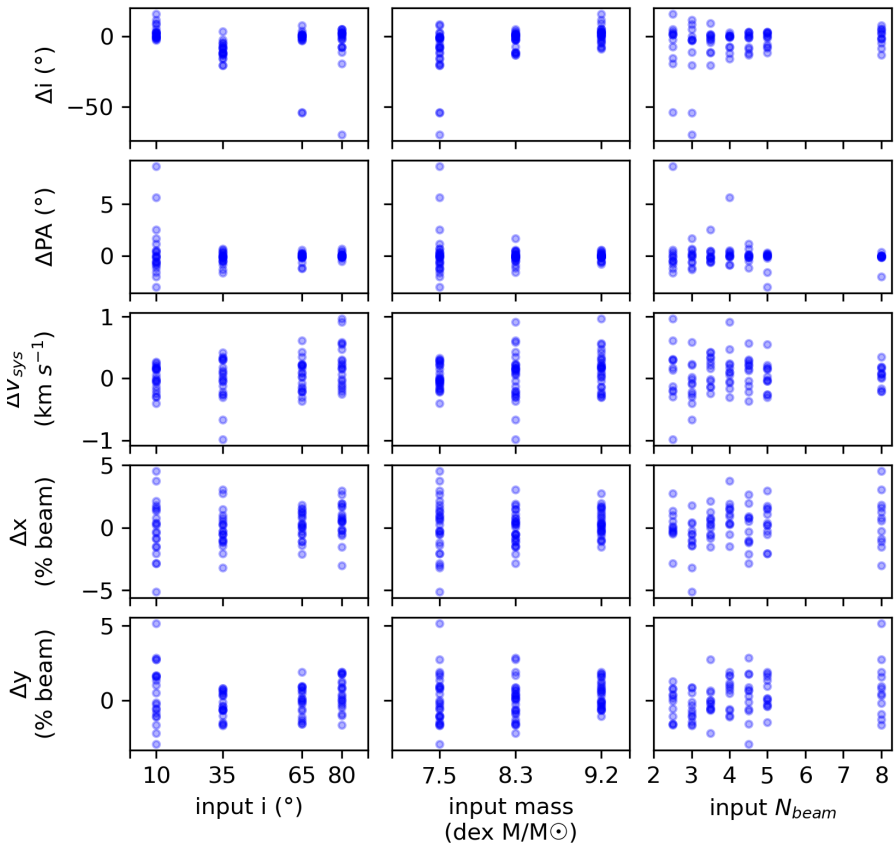

Figure 3.5: Residuals between the median recovered value and the input value for inclination (top row), position angle (second row), systemic velocity (third row), horizontal galaxy center (fourth row) and vertical galaxy center (bottom row). Each data point represents one model and each model has 50 realizations. There are 88 data points per panel. Note the y axis values and units vary from one row to another. The residuals were calculated as FAT - MCG, therefore a negative value indicates an underestimation by FAT.

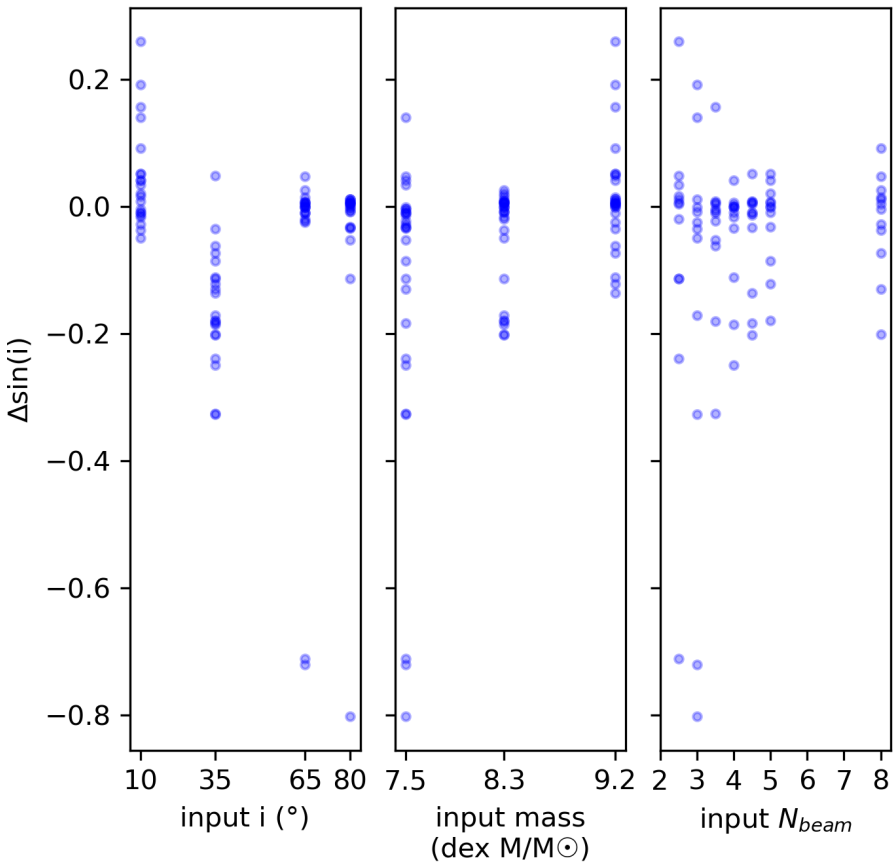

Figure 3.6: Variation in $\sin(i)$ between FAT and MCG for each base model. The FAT inclination used is the median fitted value from the 50 realizations for a given model. Note that the variation was calculated as FAT - MCG, therefore a negative value indicates an underestimation by FAT.

3.2 Modelling a WALLABY-like Sample

In this section, we test FAT's ability to retrieve the rotation curves of a realistic sample of flat axisymmetric galaxies using similar observational parameters as WALLABY.

3.2.1 Methodology

MCG's *Make_Galaxy* program (Deg and Spekkens, 2023b) was used to generate 500 unique mock observations of galaxies with parameters ranging as per Table 3.2. The distribution of the galaxy parameters is not uniform, but rather follows what is expected of observations (Koribalski et al., 2020). As such, there are more apparently small galaxies than apparently large ones (Westmeier et al., 2022; Deg et al., 2022). All galaxies were generated with an rms noise level of 1.6 mJy beam^{-1}, which is what is expected from the WALLABY survey (Koribalski et al., 2020). The fitting procedure used was the same as in section 3.1.1. The evaluation criteria followed the *by curve* analysis criteria, as a single realization was made for each galaxy. Furthermore, the inclination corrected value of the rotation curve was not calculated because the objective of this section is to determine FAT's performance on a set of WALLABY-like observations. Being the large sky survey that it is, the "true" inclination of many of the galaxies is unknown, hence inclination correction would not be possible for most galaxies.

3.2.2 Results

FAT converged on a model for 448/500 galaxies. Of the converging models, 308 were successful at recovering the rotation curve, while 140 were unsuccessful. Figure 3.7 shows the distribution of these models as a function of their input parameters. In this figure, successful models are presented as green dots, and unsuccessful models are presented as red dots.

Table 3.2: Range of parameters used to create the 500 WALLABY-like models

Parameter	Values	Units
M_{HI}	8.0 - 10.5	$M/M_{\odot}$ dex
i	15 - 90	Degrees
PA	0 - 360	Degrees
Distance	3 - 296	Mpc
N_{beam}	2.0 - 15.0	Beams across major axis

The left-most panel shows the success rate as a function of N_{beam} and M_{HI}. We can see that there are failures at all mass bins, but that the concentration of failures is far greater at low resolution than at high resolution.

The middle panel shows the success rate as a function of input i and M_{HI}. Once again, there are failures at all mass bins. However, the success rate increases drastically when going from $i < 50^\circ$ to $i \geq 50^\circ$. There are failures at high input inclinations, but are far fewer than at low inclinations.

The right-most panel of Figure 3.7 shows the success rate as a function of input inclination and spatial resolution. We notice once again a clear delineation at $i > 50^\circ$. This panel also clearly shows that the highest concentration of failures lies in the low resolution, low input inclination regime. For $N_{beam} \leq 5$ and $i \leq 40^\circ$, there are very few successes. For $N_{beam} \leq 5$ and $40^\circ < i < 50^\circ$, there is a mix of successes and failures, with many failures present. At $N_{beam} \leq 5$ and $50^\circ < i < 65^\circ$, there is still a mix of successes and failures, but the success ratio increases significantly. Finally, for $N_{beam} \leq 5$ and $i > 65^\circ$, there are only two failures. For $N_{beam} > 5$, the only clear demarcation occurs at $i = 50^\circ$. It is interesting to notice that even at the lowest resolutions evaluated ($N_{beam} = 2$), the rotation curve is well recovered for galaxies at high inclinations.

To conclude, this figure demonstrates that FAT's ability to recover the rotation curve is strongly affected by a galaxy's inclination and spatial resolution, but unaffected by its mass (at least in the mass range evaluated).

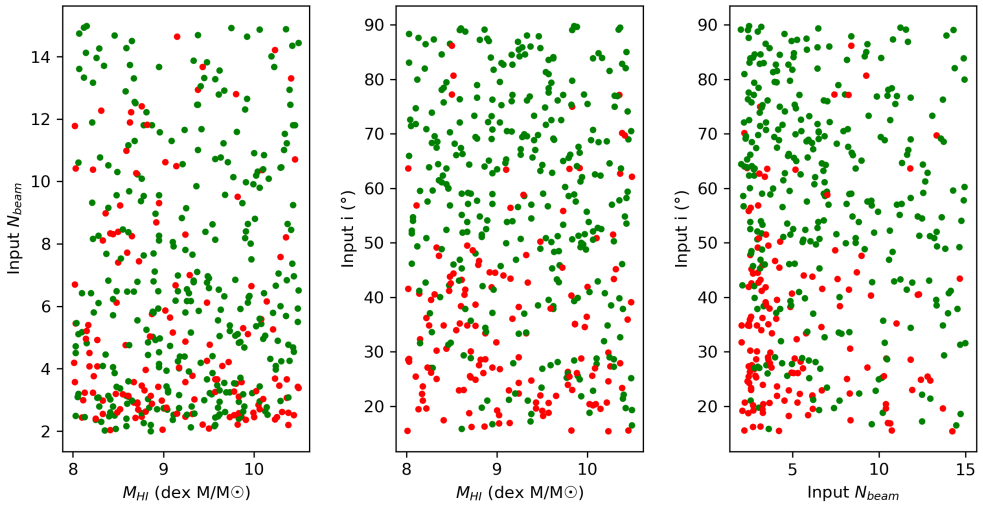

Figure 3.7: FAT model rotation curve recovery for the 500 WALLABY-like flat disk sample. Successful models are shown in green, while unsuccessful models are shown in red. The left panel shows the success rate as a function of N_{beam} and M_{HI}; the middle panel shows the success rate as a function of input i and M_{HI}; and the right panel shows the success rate as a function of input i and input N_{beam}. FAT models that did not converge to a solution are not plotted; there are therefore 448 data points per panel.

3.3 Conclusion

We have evaluated FAT's ability to recover the rotation curve of a galaxy using three methods. First we performed a *by curve* analysis on 50 realizations of various underlying models. Second, we performed a *bin median* analysis on the same set of models. Lastly, we performed the *by curve* analysis on a sample of 500 unique mock galaxies. The two first evaluation methods allowed us to conclude that FAT can reliably recover the rotation curve for flat axisymmetric galaxies at $N_{beam} \geq 2.5$ when $i \geq 65°$ and $M_{HI} \geq 8.3\,\mathrm{dex}\,M/M_{\odot}$. The results are however not precise limits as the parametric variations were large from one model to the next (i.e. going from an $i = 35°$ to $i = 65°$). As such, we fine tuned FAT's limitations using the third evaluation process. This lead us to the final conclusion that FAT is able to accurately recover the rotation curve of galaxies of $M_{HI} \geq 8\,\mathrm{dex}\,M/M_{\odot}$ if

a) $N_{beam} \geq 2$ and $i \geq 65°$; or

b) $N_{beam} \geq 5$ and $i \geq 50°$.

Chapter 4

FAT Models of Warped Disks

In Chapter 3, we have analysed the Fully Automated TiRiFiC's (FAT) performance on flat disks. With this baseline analysis in hand, we will now perform an evaluation on warped galaxies. In section 4.1, we will describe how we created data cubes for warped galaxies using MCG. In section 4.2 we will analyse FAT's ability to retrieve the rotation curve and galaxy geometry by letting the fitting code vary its parameters radially. In section 4.3, we will force FAT to fit flat models to warped galaxies in order to determine how this will affect FAT's ability to recover the rotation curve. We will also compare them to our flat models of flat disks (from section 3.2) in section 4.4. In section 4.5 we will discuss our findings, and we will summarize them in section 4.6.

4.1 Generating Warped Galaxies

At the time of writing this thesis, the MCG_Suite programs did not have the ability to generate warped galaxies. This capacity had to be added for the purpose of this analysis. In order to do so, a new version of the Make_Galaxy program was created by Dr. Nathan Deg. As mentioned in section 2.5 the program first creates a set of rings in the galaxy plane, populates it with gas cloudlets then projects it on the sky based on the observation parameters specified by the user. Ideally, the warps would have been created in the galaxy plane then projected in the sky. However, due to time constraints, a simpler approach was taken in which the disk inclination and position angle are modified in sky plane. These approaches are not exactly equivalent as projection effects would modify the perceived warp when built in the galaxy plane. Went the warp is built in sky plane, we see it exactly as it was generated. In order to generate warps in the galaxy plane, a Euler formalism would need to be implemented in the code.

Table 4.1: Range of values used to generate warped galaxies

Parameter	Value at $r = 1.5R_{HI}$	Value at $r = R_{HI}$	Units
$R_{warpstart}$	0.3 - 0.6	0.3 - 0.6	fraction of R_{HI}
Δi	10 - 30	0 - 30	Degrees
ΔPA	30 - 70	0 - 61	Degrees

In order to create warps in this manner, three new parameters were added to the MCG input file: $R_{warpstart}, PA_{end}, Inc_{end}$. $R_{warpstart}$ refers to the radius at which the warp begins. This is the same as r_w used in other studies. PA_{end} and Inc_{end} refer to the values of the position angle and inclination at the outermost point of the galaxy disk, which corresponds in MCG to $r = 1.5\,R_{HI}$, where R_{HI} is the radius at which the HI column density drops below $1\mathrm{M}_{\odot}\mathrm{pc}^{-2}$.

For the main analysis of this paper, warps were generated by making the position angle and inclination vary as x^3. To be clear, the inclination and position angle are constant from r=0 to $r = R_{warpstart}$, at which point they start varying as x^3 to reach their final value (PA_{end} and Inc_{end}) at $r = 1.5\,R_{HI}$. The warps were generated this way because, after having fit the parameters, FAT smooths the inclination and position angle to a polynomial of order 0, 2, 3, 4 or 5 (Kamphuis et al., 2015). We decided to generate the warps as x^3, the middle value of the possible smoothing process values.

Using this method, a suite of 500 symmetrically warped disk models was generated. Although perfectly symmetrically warped galaxies are rare, this is a good approximation in many cases (the warps of Figures 2.1 and 2.2 are quite symmetric). Each warped model was generated by taking the corresponding flat disk model and adding a warp with a start radius and a variation in inclination and position angle randomly drawn from the limits set in Table 4.1. These limits resulted in warps with values varying between $0° < \Delta i < 30°$ and $0° < \Delta PA < 61°$ for radii between $15" < r \leq R_{HI}$. Where $\Delta i = i(r = R_{HI}) - i(r = 0)$ and $\Delta PA = PA(r = R_{HI}) - PA(r = 0)$. Note that we are not using the α and β angles (Section 2.2), but rather directly using i and PA. We do however believe that these parameters represent realistic warps. The generated warps correspond in size to what is observed albeit on the larger end of the spectrum. This was done purposefully as it is expected that smaller warps should affect the rotation curve less than larger ones. Analysis of this sample will be discussed in sections 4.2 and 4.3.

One may wonder what happens if a galaxy contains a warp that cannot be accurately represented by a polynomial fit of order 0, 2, 3, 4 or 5. We have

briefly investigated this scenario. To do so, we generated warps by varying the inclination and position angle with polynomials of order 1 and 1/2. The FAT recovered values for 50 realizations of an underlying model can be seen in Figures 4.1 and 4.2. As can be seen by the blue lines of panels c) and d) in Figure 4.1, FAT often fails to identify a change in inclination and position angle when their value changes linearly. When FAT identifies the change, it fails to find the correct shape. This can be seen by comparing a given blue curve to the input curve (red). Similar, but worse results are seen when the warp is generated using a square root variation (see Figure 4.2). This means that if a warp has a sharp onset with a gradually diminishing variation FAT will have great difficulty modelling it.

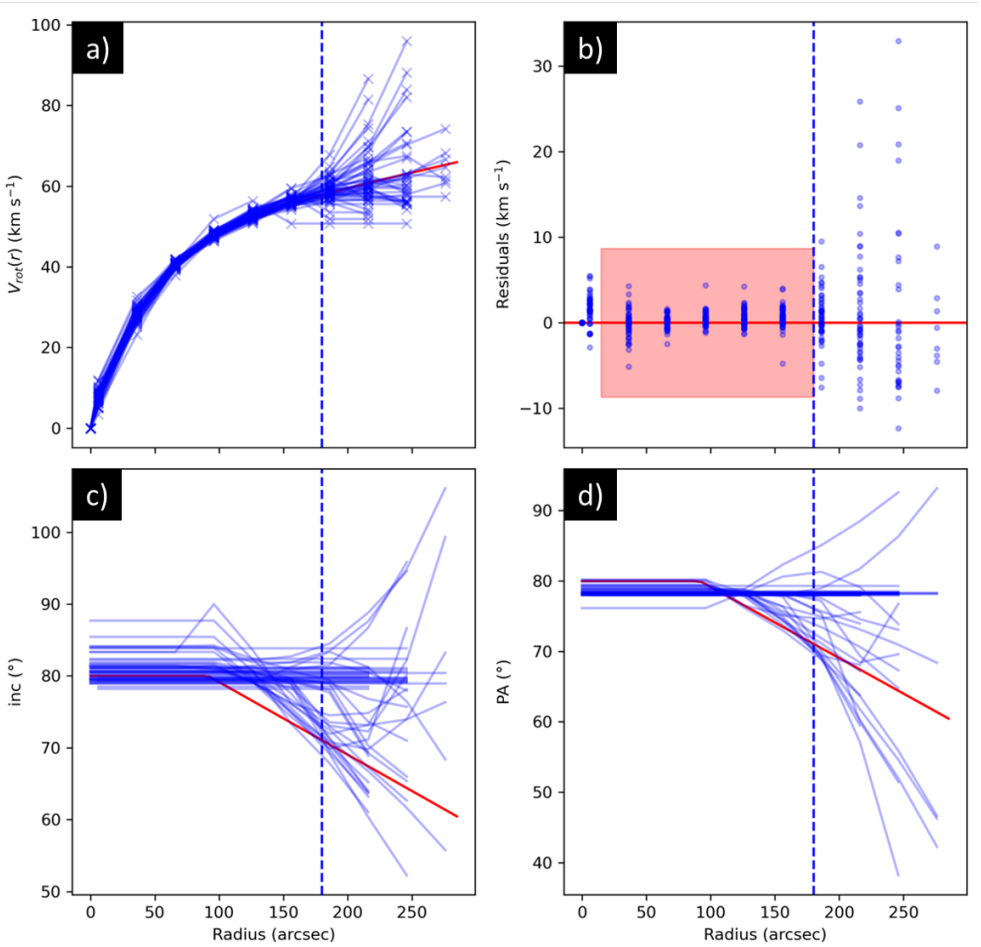

Figure 4.1: FAT recovered rotation curves (panel a); residuals between the FAT recovered rotation curve and the input (panel b); FAT recovered values for the inclination (panel c); and FAT recovered values for the position angle (panel d) for a mock galaxy containing a warp exhibiting a linear variation in inclination and in position angle in the warp region. Blue lines show the values as recovered by FAT. Red lines show the input value. The dashed blue line shows $r = R_{HI}$. The red shaded area represents the "acceptable fit zone" as described in section 3.1.1.

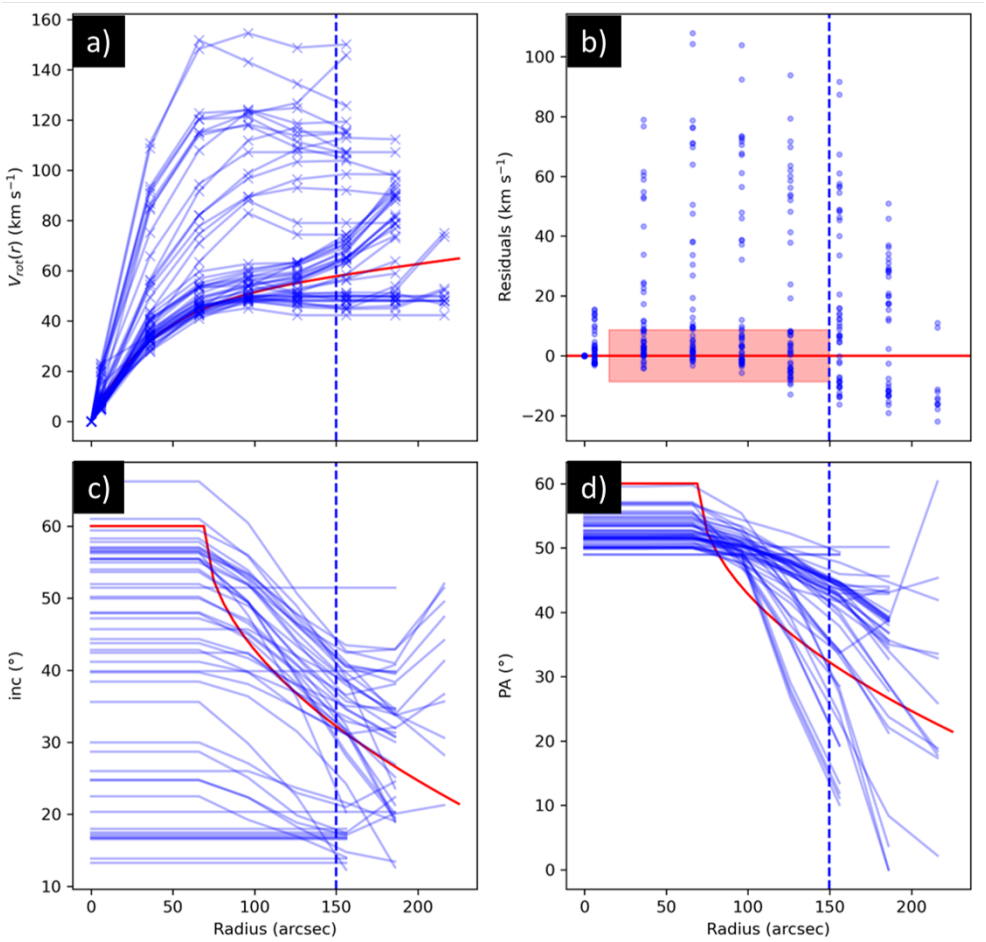

Figure 4.2: FAT's recovery of the rotational velocity, inclination and position angle for a galaxy containing a warp exhibiting a square root variation in inclination and in position angle in the warp region. Points, lines and shaded areas are the same as in Fig 4.1.

4.2 Warped Models of Warped Disks

In this section, we make use of FAT's ability to create models with radially varying parameters. This mode allows the position angle and inclination to vary radially and evaluates the approaching and receding sides separately. Note the rotational velocity is not separated in approaching and receding sides. We will use this "variable fitting mode" to see if FAT shows the same level of performance than it did for flat disk galaxies and we will investigate under which conditions it finds a symmetric warp.

4.2.1 Methodology

First, we have identified a series of questions to determine all possible outcomes from the fitting process of a galaxy. These questions can be found in Figure 4.3. The flowchart was developed in such a way that each FAT model of a mock galaxy realization can only fall into one category. The flowchart asks the following questions, in this order:

1. *Did the model converge?* This is a simple yes or no question. If FAT generated a model for the galaxy, the answer to this question is yes;

2. *Did FAT fit a warp?* We considered FAT as having fit a warp if one of the sides of either the inclination or position angle varied. This question was split in three possible answers: yes; no with $N_{beam} \geq 6.0$; and no with $N_{beam} < 6.0$ because FAT only fits warps for galaxies that it measures as having an $N_{beam} \geq 6.0$ (see section 2.4). It is therefore expected that no galaxy with an angular size below this will be identified by FAT as being warped;

3. *Are the recovered inclination and position angle accurate?* If the recovered inclination and position angle, for both approaching and receding sides, are within 5° of the input value between 15" $< r <$ R_{HI}, we consider them successfully recovered. We chose this value to differentiate between models that fail to recover the rotation curves because of a misetimated i/PA from those that fail due to other reasons. This is a particularly stringent criterion as even for flat disks, FAT models regularly do not recover the i/PA to this level of precision (see Chapter 3).

4. *Was the rotation curve accurately recovered?* Success was based on the *by curve* analysis as described in Chapter 3.

Second, we ran the 500 warped models through FAT using the "variable fitting mode". Upon completion of the fitting run, the total number of models corresponding to each category was tallied as shown in Figure 4.3. A visual representation of the analysis of a mock galaxy is presented in Figure 4.4. In this figure, the red line shows the input value; cyan and magenta represent the FAT recovered approaching and receding sides respectively; and blue is used for non side specific data. The top row shows the rotation curve (left) and its residuals (right); the middle row shows the inclination (left) and its residuals (right); and the bottom row shows the position angle (left) and its residuals (right). The light red region shows the "acceptable fit zone" for each parameter.

Third, we assessed whether or not each model's rotation curve was successful and whether or not its warp was identified, as a function of input parametric values. This will allow us to find which parametric combinations allow successful modelling. Results can be seen in Figure 4.5.

Finally, we assessed the impact of the strength of the warp on its modellability. In this test, the total strength of the warp is defined as the variation in position angle plus the variation in inclination ($\Delta PA + \Delta i$), measured between $r = 0$ and $r = R_{HI}$. A plot of the entire sample showing whether each model's rotation curve was successful or not and whether its warp was identified or not, as a function of warp strength can be seen in Figure 4.6.

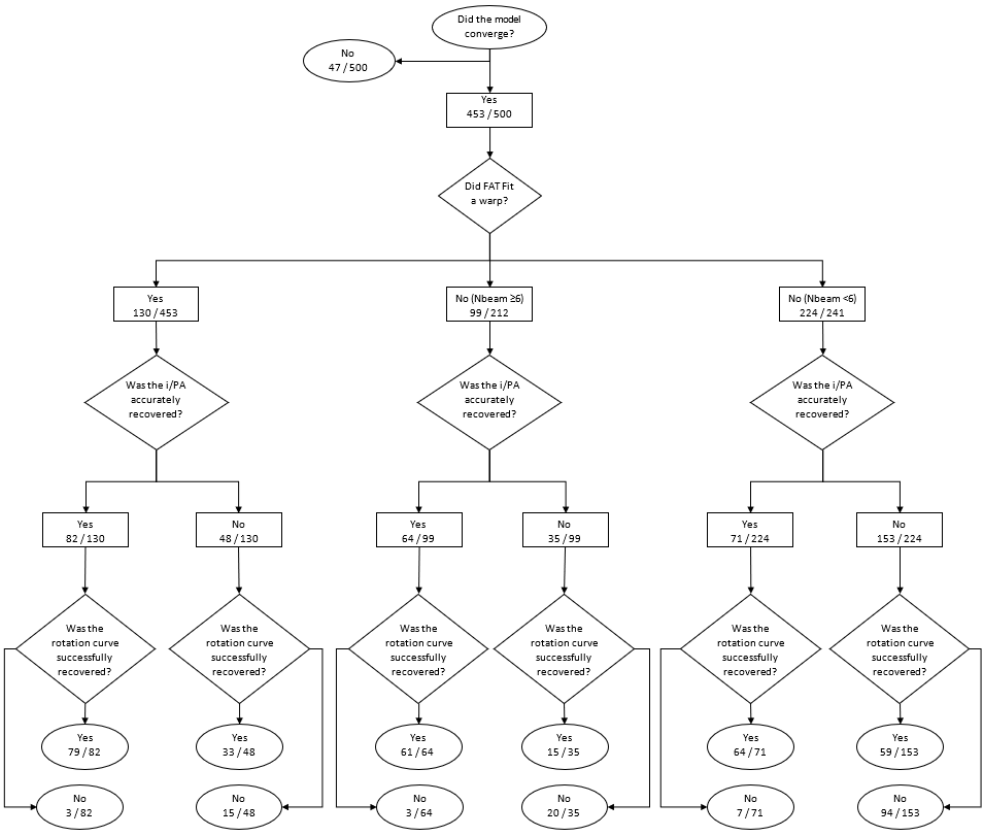

Figure 4.3: Flow chart showing the process followed to separate the recovered models by category based on possible FAT outcomes. For each possible category, the process finishes by asking whether the rotation curve was accurately recovered or not. The fraction of galaxies falling in each category is indicated in each box.

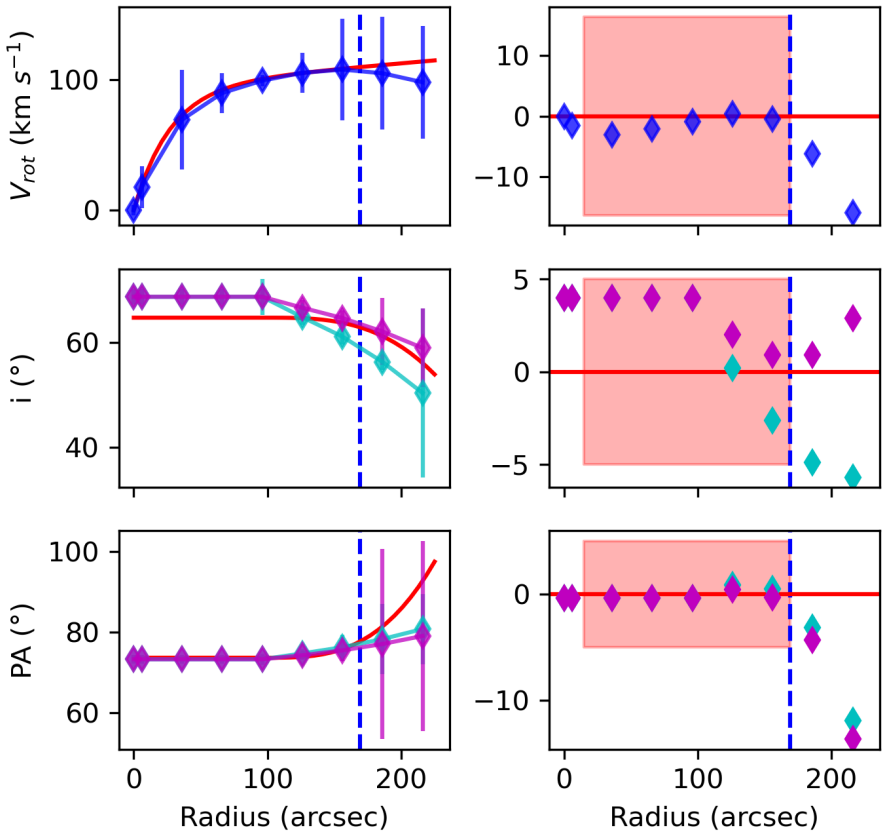

Figure 4.4: Sample diagnostic plot for a warped galaxy. The left column shows the absolute recovered values, while the right column shows the residuals between the recovered value and input value. The top row shows the recovered (blue) and input (red) rotational velocity. The middle row shows the recovered approaching side (cyan), receding side (magenta) and input (red) inclination. The bottom row shows the recovered approaching side (cyan), receding side (magenta) and input (red) PA. The blue dashed line indicates R_{HI} and the red shaded area represents the "acceptable fit zone".

4.2.2 Results

Flowchart

Our first set of results stem from answering the questions in Figure 4.3. As can be seen, 47/500 models failed to converge to a solution. Of the converging models, FAT identified the presence of a warp 130/453 times. Of these 130 models, the inclination and position angle were accurately recovered 82/130 times (63%). When this was the case, the rotation curve was accurately recovered 79/82 times (96%). Alternatively, FAT identified the presence of a warp, but failed to properly recover the inclination and position angle 48/130 times. In this case, the rotation curve was successfully modelled 33/48 times (69%).

FAT failed to identify a warp 323/453 times. Remember though that FAT only fits warps to galaxies having $N_{beam} \geq 6.0$. 211 generated models met this criterion. However the angular size as measured by FAT from a datacube is different from the angular size that the user inputs into MCG. As such, we investigated the number of galaxies as a function of the angular size as determined by FAT. We found that FAT identified 212 galaxies as having $N_{beam} \geq 6.0$; and 241 galaxies as having $N_{beam} < 6.0$. Therefore, FAT failed to identify a warp in galaxies with a FAT $N_{beam} \geq 6.0$ 99/212 times. Furthermore, FAT failed to identify the warp in galaxies with FAT $N_{beam} < 6.0$ 224/241 times. This means that FAT identified a warp in 17/241 galaxies with $N_{beam} < 6.0$. This is very surprising. We expected 0 warps to be identified in this regime since FAT does not fit warps for $N_{beam} < 6.0$. Perhaps the reason these warps were identified is because the initial estimates put the mock galaxy at an $N_{beam} > 6$ and later iterations of TiRiFiC reduced their size to below this value.

In the group of 99 unidentified warps (with $N_{beam} \geq 6.0$), the i/PA was well recovered 64/99 times. Of these, the rotation curve was successfully recovered 61/64 times. Alternatively the i/PA was not well recovered 35/99 times. Of these, the rotation curve was successful only 15/35 times.

In the group of 224 unidentified warps (with $N_{beam} < 6.0$), the i/PA was accurately recovered 71/224 times. In this case, the rotation curve was successfully recovered 64/71 times. Alternatively the i/PA was unsuccessfully recovered 153/224 times. In this case, the rotation curve was successful only 59/153 times.

These results show that regardless of whether or not the warp is recovered, the rotation curve has a high probability of being accurately recovered only when the inclination and position angle are well recovered. If either of these parameters is not well recovered, the probability of recovering the ro-

tation curve decreases significantly. There are several instances when either the inclination and/or PA are not well recovered, but the rotation curve is still successful. In this case, we suspect the other parameters to be very well recovered.

Diagnostic Plot

Figure 4.5 shows successfully (green) and unsuccessfully (red) recovered rotation curves, and whether or not the warp was identified (squares) or not (crosses) as a function of M_{HI}, the FAT recovered N_{beam} and input i. In the left panel, we compare the galaxy's angular size as a function of its HI mass. We see no clear correlation between success rate and M_{HI}, but notice more failures are present at lower resolutions than at higher resolutions. As expected, very few warps are identified at $N_{beam} < 6$. There seems to be no correlation between warp identification and HI mass.

The center panel of Figure 4.5 plots input i as a function of M_{HI}. Note that the input inclination depicted here refers to the inclination of the flat, inner portion of the galaxy as generated in MCG. We notice a drastic increase in the success rate when going from $i < 50^{\circ}$ to $i \geq 50^{\circ}$, consistent with our results for flat disk galaxies (Chapter 3). Once again there are failures at all mass bins. FAT's ability to recover the warp does not seem to depend on M_{HI}, however may be affected by input i: the number of identified warps is proportionally larger at high inclinations.

In the right panel of Figure 4.5, we compare input i and FAT recovered N_{beam}. In this plot, we clearly notice the high failure rates in the low resolution, low inclination regime (as was expected from the discussion of Chapter 3). We also notice that FATs ability to recover the warp is highly dependent on spatial resolution: the density of crosses is very high at low N_{beam} but decreases as N_{beam} increases. Furthermore, more warps are identified at high inclination than at low inclination. As expected, there are almost exclusively crosses at $N_{beam} < 6$ as FAT does not try to fit warps at these resolutions. However, it is interesting to see that there are unidentified warps at $N_{beam} > 10$. This may be because the warps are small or because the noise prevented their recovery. This will be investigated shortly.

In sum, we can draw two main conclusions from Figure 4.5. First, the regimes in which the rotation curves are successfully recovered are similar whether the galaxy contains a warp or not (see Chapter 3). Second, FAT's ability to identify a warp is highly dependent on resolution, somewhat affected by input inclination, and unaffected by input HI mass (for the mass range evaluated).

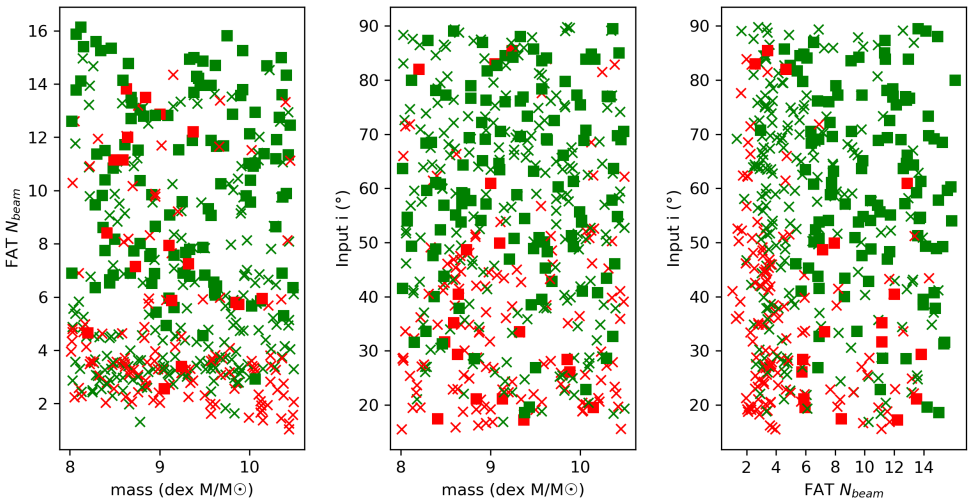

Figure 4.5: Rotation curve recovery and warp identification for a sample of 500 warped galaxies. Only models that converged to a solution are plotted, therefore there are 453 data points per panel. Successfully recovered rotation curves are shown in green; unsuccessfully recovered rotation curves are shown in red. Squares identify models for which a warp was identified and crosses identify models for which the warp was not identified by the FAT model. The input inclination depicted here is the value for the inner (flat) part of the galaxy and the N_{beam} is that as evaluated by FAT.

Warp Strength

We have so far identified the spatial resolution as the most important factor in FAT's ability to identify the presence of a warp, however the strength of the warp obviously has its role to play as well. To explore this possibility, we started by investigating the variation in inclination and position angle separately, but no significant results were found. More interesting was the total strength of the warp, defined as $\Delta i + \Delta PA$. Results can be seen in Figure 4.6.

Galaxies for which the warp was identified, but the rotation curve failed (red squares) are generally located in the low warp strength regime, indicating that FAT is able to identify the existence of small warps, but has difficulty finding their value.

Galaxies for which a warp is identified and the rotation curve is successful (green squares) are generally located in the stronger warp, higher resolution regime, which is not surprising as this is the regime in which FAT's estimates are best. Contrary to what was expected, many models that successfully recovered the rotation curve, but failed to identify the warp (green cross) are also found in the large warp, high resolution regime. This means that despite having significant warps, FAT was unable to identify them. The fact that their rotation curve was well recovered indicates that the inclination and position angle of the flat disk were well estimated. Furthermore, their recovered value most likely lies between the true value of the inner and outer disks. If this is the case, it means that during its first fitting process, FAT tries to fit an average value to the galaxy as a whole.

Surprisingly, there are galaxies for which FAT fit a warp despite having identified them as having $N_{beam} < 6$. Once again, this is very strange as FAT is not meant to fit warps at these resolutions. As is to be expected though, the vast majority of models with $N_{beam} < 6$ did not fit a warp. Similarly, it is natural to see many unidentified warps in the low warp strength region, as modest warps are more difficult to find.

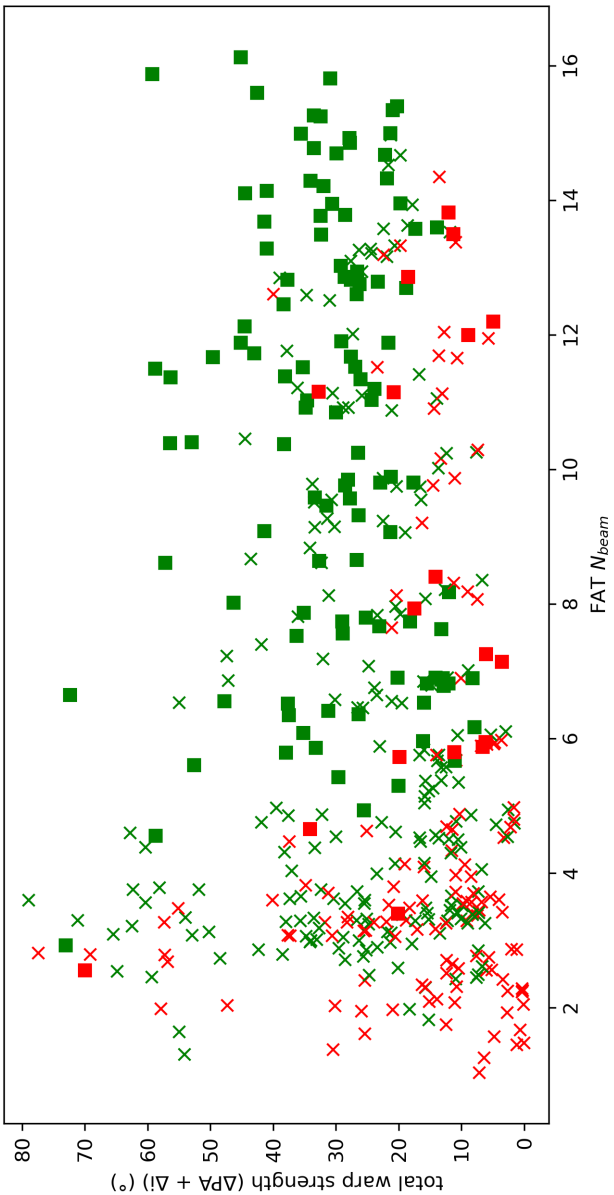

Figure 4.6: Rotation curve recovery as a function of warp strength. Colours and markers follow the same format as Figure 4.5.

4.3 Flat Models of Warped Disks

In the previous section, we fit warped models to warped galaxies by letting FAT vary its parameters radially. In this section, we will force FAT to fit a flat disk to a warped galaxy. This will allow us to determine how well the rotation curve of a warped galaxy can be approximated using a flat disk. This is particularly interesting because in current literature authors fit flat models to HI disks, despite the fact that HI disks are often warped. If there is a large discrepancy between the flat models and the idealized warped disks generated here, there must also be large discrepancies between flat models and observed HI disks. Our previous study indicates that FAT often missed the warp and hence fits a flat disk. We therefore expect the flat models to represent warp disks quite well. If this is the case, the current process of using flat models of warp disks could be continued. In this case, we would have the benefit of reduced computational times as fitting flat models is less computational demanding than fitting warped models.

4.3.1 Methodology

This section uses the same evaluation criteria to determine the accuracy of the rotation curve as the previous sections: the rotation curve is deemed accurate if all data points between 15" $< r \leq R_{HI}$ are within 15% of the input V_{rot} value at R_{HI}. The sample used for this test is the same one as in section 4.2.

4.3.2 Results

Of the 500 models, 450 converged to a solution. The number of galaxies for which the model found an acceptable rotation curve was 300/450. Figure 4.7 shows the parameters of the 450 converged models and whether their rotation curve was successfully recovered (green) or not (red). In the left panel, we plot rotation curve recovery as a function of M_{HI} and N_{beam}. From this panel we can see there are failures at all N_{beam}, but the proportion of failures is higher at lower N_{beam}. We see no correlation between the input M_{HI} and failure rate.

In the center panel of Figure 4.7, we plot the input i as a function of input M_{HI}. We notice the failure rate is much higher at low i, and decreases drastically at $i = 50°$. Once again, we see no correlation between M_{HI} and failure rate.

The right panel of Figure 4.7 shows the success rate as a function of N_{beam} and input i. We could split this panel in three general areas. The first area is the low resolution, low inclination regime ($i < 50°$ and $N_{beam} \leq 4$). This area

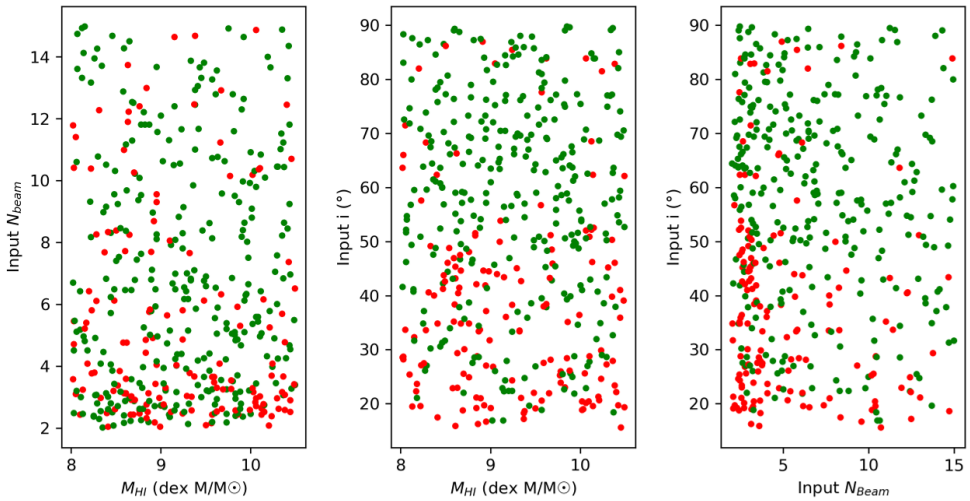

Figure 4.7: Rotation curve recovery of 500 warped mock galaxies, fit with a flat model. Only models that converged to a solution are plotted, therefore there are 450 data points per panel. This figure follows the same format as Figure 3.7, with green points denoting a successful recovery and red points denoting an unsuccessful recovery. Note the inclination depicted here is that of the the flat inner part of the galaxy as generated in MCG.

contains by far the highest concentration of failures. The area containing the second highest failure rate is the area at $i < 50°$ and $N_{beam} > 4$. In this area there is a mix of successes and failures in roughly equal distribution. Finally, at $i \geq 50°$ the success rate is very high. This is very much in line with what was found in our previous evaluations (see Figures 4.5 and 3.7).

4.4 Comparing Flat Models of Flat Galaxies and Flat Models of Warped Galaxies

Our final test consists of comparing the success rates from flat models of flat galaxies to those of flat models of warped galaxies. As previously mentioned, the 500 warped galaxies were generated by adding a warp to the same base model as an existing mock flat disk galaxy. In doing so, all 500 warped galaxies have a flat counterpart allowing us to easily compare the two. The results are given in Table 4.2 and Figure 4.8.

Table 4.2 shows that the FAT fits to the two samples performed extremely similarly. For the flat galaxies, 448/500 converged to a solution with 308/448 successfully recovered rotation curves; for the warped galaxies, 450/500 con-

Table 4.2: Comparing FAT's performance using flat models on flat disks and using flat models on warped disks

	Flat models of flat disks	Flat models of warped disks
# converging models	448/500	450/500
# Successfully recovered rotation curves	308/448	300/450

verged to a solution, with 300/450 successfully recovered rotation curves. Very clearly, the two samples behave almost identically and, as can be seen in Figure 4.8, the regions in which the models are unsuccessful are the same. Both have most difficulty in the low resolution, low inclination regime and show a drastic increase in performance at $i > 50°$.

As such, we find that fitting flat models to warped galaxies provides a good estimate for the rotation curve. We must, however, be very careful with this statement as this is only true for radii $15" < r \leq R_{HI}$ for warps that behave like those generated in this thesis.

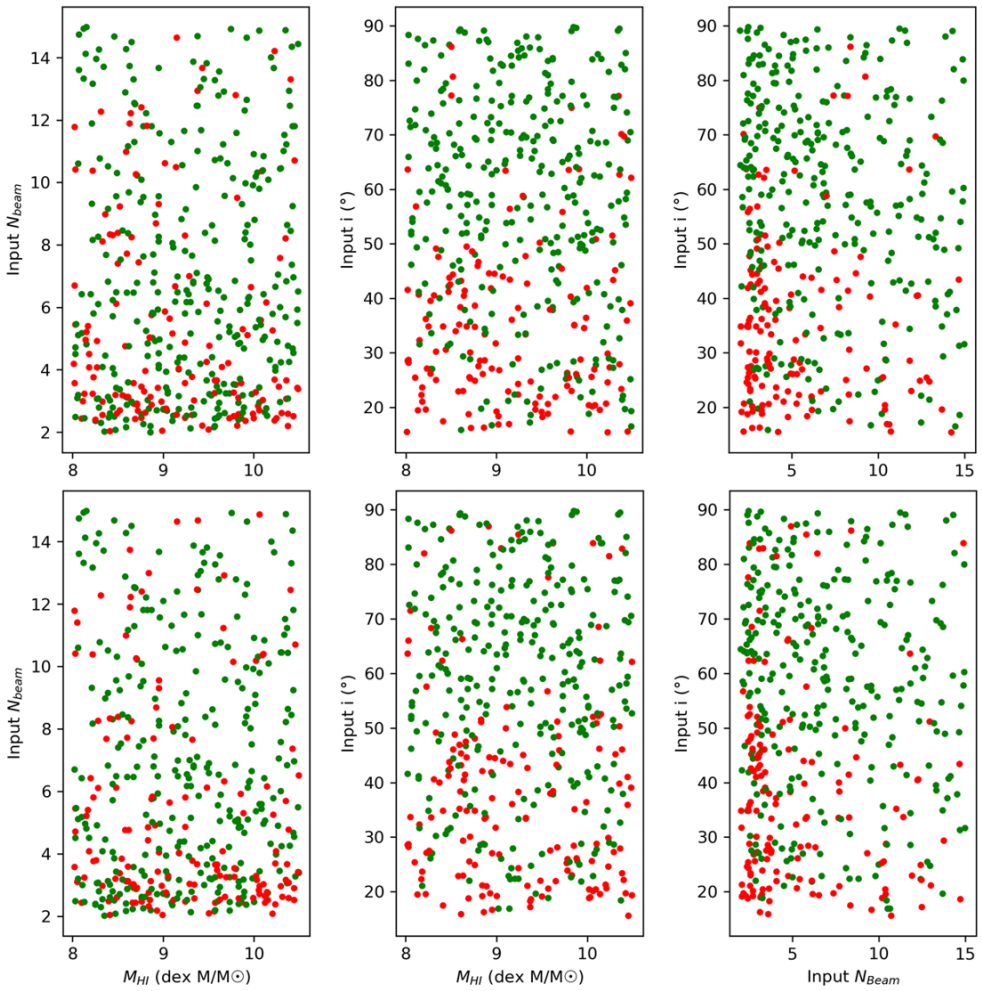

Figure 4.8: Comparison between flat models of flat disks (top) and flat models of warped disks (bottom). Only converging models are plotted, there are therefore 448 data points per panel in the top row and 450 data points per panel in the bottom row. Note the similarity between the results of these two samples. The colour scheme follows that of Figure 3.7.

4.5 Discussion

The results presented above are very interesting, however there are several considerations to note before applying them to a larger context. First, the way we generated warps (in disks that are themselves ideal) only considers one possible configuration. Our warps have an inclination and position angle that vary as x^3 in sky plane. Furthermore, they vary in one direction only (they do not contain a wiggle) and they are not truncated. Second, the rotation curve was only evaluated for radii $15" < r \leq R_{HI}$. These radial limits are often sufficient, however, future studies may chose a different radial range in which flat disks no longer give a good approximation. Third, the warps we created vary between $0° < \Delta i < 30°$ and $0° < \Delta PA < 60°$ in the radial range evaluated. This is in line with current literature on warp strength (Ann and Park, 2006; García-Ruiz et al., 2002; Sánchez-Saavedra et al., 2003), however it is uncertain whether our results will remain valid for warps larger than this.

Additional notes on our results: first, for galaxies with $N_{beam} \leq 2.3$, there was a single data point within $15" < r \leq R_{HI}$. When examined by eye, the models that failed to recover the rotational velocities also failed to recover the rotation curve shape. For the models that successfully recovered the rotational velocity value, the data points outside the evaluated range followed the shape of the input rotation curve. As such, we considered all models with $N_{beam} \leq 2.3$ valid and included them in our sample analysis.

Second, we noticed that FAT's ability to accurately recover the inclination and position angle sometimes had a larger impact on its ability to recover the rotation curve than the warp did. This occurred when the deviation between FAT's estimate and the input value for i or PA was larger than the $\Delta i/\Delta PA$ caused by the warp. This is mainly the case for low inclination and low resolution galaxies, for which the i/PA recovery is more difficult.

4.6 Conclusion

In this chapter, we performed three tests. First we evaluated FAT's ability to fit warped galaxies by letting the algorithm vary the model's ring parameters radially. FAT demonstrated similar performance to the case when it fits flat galaxies. Furthermore, it was found that FAT:

a) occasionally fit warps to galaxies with $N_{beam} < 6$;

b) was able to find warps with small warp strengths, but often failed to recover their rotation curve;

c) identifies the presence of a warp more easily when the galaxy has a higher resolution and when a strong warp is present; and

d) regularly failed to identify the presence of a warp: even at $N_{beam} \geq 10$.

Second, we forced FAT to fit flat models to warped galaxies. We found FAT's ability to recover the rotation curve showed similar behavior to that during our other tests.

Finally, we compared the results from fitting flat models of flat galaxies to those from fitting flat models to warped galaxies. It was found that both sets of models behaved extremely similarly. The rotation curves were accurately recovered for roughly the same fraction of galaxies, and both samples failed for the same parametric combinations.

We can thus conclude that by fitting flat models to warped galaxies, we can obtain good estimates of their rotation curve. As such, for the purpose of large sky surveys, flat models should be used, as they provide statistically accurate rotation curves, while saving computational time. This is however only valid for the type of warp presented here. Other warp shapes and amplitudes may yield different results.

Chapter 5

Conclusion

Current large sky HI survey often produce marginally resolved detections. Performing science on marginally resolved galaxies is difficult as their spatial resolution is limited, making accurate analyses difficult. It is however important to attempt to model these galaxies as they can provide statistically meaningful results. At present, flat disk models are used to characterize marginally resolved HI disks, however it is known that HI disks are warped (García-Ruiz et al., 2002). No one has investigated the effects of modelling marginally resolved warped HI disks with flat models until today.

This thesis began with an analysis of the Fully Automated TiRiFiC's (FAT) ability to recover the rotation curves of marginally resolved galaxies. It was found that FAT is able to accurately recover the rotation curve of galaxies with $M_{HI} \geq 8.0$ dex if a) their $N_{beam} \geq 2.0$ and $i \geq 65°$; or b) their $N_{beam} \geq 5.0$ and $i \geq 50°$.

The second analysis consisted in evaluating FAT's performance when letting the models vary radially on a set of 500 warped galaxies. FAT demonstrated a similar ability in recovering the rotation curve than it did on flat galaxies. Once again, the low resolution, low inclination galaxies were hardest to fit. Rotation curves were occasionally successful at $i < 50°$, but the success rate increased drastically for $i \geq 50°$. Furthermore, we learned about FAT's ability to identify the presence of a warp. We learned that a) FAT occasionally identifies the presence of a warp for galaxies with $N_{beam} < 6$; b) FAT is able to find mild warps, but often fails to recover their host galaxy's rotation curve; and c) FAT has some difficulty identifying the presence of a warp in the regime evaluated here: 130/212 galaxies with $N_{beam} \geq 6.0$ were identified as containing a warp.

Finally, when comparing FAT's ability to recover the rotation curve of warped galaxies using flat disk models, FAT was found to be extremely suc-

cessful. As a matter of fact the rotation curves of 300/450 galaxies were successfully recovered. These results are practically identical to when recovering the rotation curves of flat disk galaxies (308/448). As such it is recommended to continue using flat disk models to recover the rotation curves during untargetted surveys such as WALLABY and those of the future SKA. This thesis has shown flat disk models provide a good approximation for the rotation curve of warped HI disks, while saving numerous computational hours.

It is, however, important to note that the above results are strictly valid for the symmetric warps in the idealized mock galaxies studied here.

Planned future work includes completing a similar analysis for truncated warps and U shaped warps, an in-depth analyses of a strongly warped mock galaxy, and smoothing down real observations of warped galaxies until they are marginally resolved and test FAT on them. The truncation present in some galaxies and the shape of the warp (U as opposed to S) may decrease the algorithms ability to properly recover the galaxy parameters. An in-depth analysis of a strongly warped disk will allow us to determine FAT's ability to recover all parameters, not only the rotation curve. Finally, smoothing observational data would create a much more realistic sample, allowing us to determine FAT's limitations on observed galaxies.

Bibliography

Elizabeth Adams, Björn Adebahr, Willem JG de Blok, Kelley M Hess, Danielle M Lucero, Filippo Maccagni, Raffaella Morganti, Tom A Oosterloo, Anastasia Ponomareva, Lister Staveley-Smith, et al. Apertif: A new phased-array feed for WSRT. In *American Astronomical Society Meeting Abstracts# 231*, volume 231, pages 354–04, 2018.

HB Ann and J-C Park. Warped disks in spiral galaxies. *New Astronomy*, 11 (4):293–305, 2006.

D. G. Barnes, L. Staveley-Smith, W. J. G. de Blok, T. Oosterloo, I. M. Stewart, A. E. Wright, G. D. Banks, R. Bhathal, P. J. Boyce, M. R. Calabretta, M. J. Disney, M. J. Drinkwater, R. D. Ekers, K. C. Freeman, B. K. Gibson, A. J. Green, R. F. Haynes, P. Te Lintel Hekkert, P. A. Henning, H. Jerjen, S. Juraszek, M. J. Kesteven, V. A. Kilborn, P. M. Knezek, B. Koribalski, R. C. Kraan-Korteweg, D. F. Malin, M. Marquarding, R. F. Minchin, J. R. Mould, R. M. Price, M. E. Putman, S. D. Ryder, E. M. Sadler, A. Schröder, F. Stootman, R. L. Webster, W. E. Wilson, and T. Ye. The HI parkes all sky survey: southern observations, calibration and robust imaging. *Monthly Notices of the Royal Astronomical Society*, 322(3):486–498, 2001.

E Battaner, E Florido, and ML Sanchez-Saavedra. Intergalactic magnetic field and galactic warps. *Astronomy and Astrophysics (ISSN 0004-6361), vol. 236, no. 1, Sept. 1990, p. 1-8.*, 236:1–8, 1990.

K. G. Begeman. *HI rotation curves of spiral galaxies.* PhD thesis, Kapteyn Institute, 1987.

James Binney. Warps. *Annual review of astronomy and astrophysics*, 30(1): 51–74, 1992.

Albert Bosma. *The distribution and kinematics of neutral hydrogen in spiral galaxies of various morphological types.* PhD thesis, Rijksuniversiteit te Groningen., 1978.

FH Briggs. Rules of behavior for galactic warps. *The Astrophysical Journal*, 352:15–29, 1990.

Aaron Chippendale, John O'Sullivan, John Reynolds, Russell Gough, Douglas Hayman, and Stuart Hay. Phased array feed testing for astronomy with ASKAP. In *2010 IEEE International Symposium on Phased Array Systems and Technology*, pages 648–652. IEEE, 2010.

W. J. G. de Blok, F. Walter, E. Brinks, C. Trachternach, S-H. Oh, and R. C. Kennicutt. High-resolution rotation curves and galaxy mass models from THINGS. *The Astronomical Journal*, 136:2648, 2008.

N Deg, K Spekkens, T Westmeier, TN Reynolds, P Venkataraman, S Goliath, AX Shen, R Halloran, A Bosma, B Catinella, et al. WALLABY pilot survey: Public release of HI kinematic models for more than 100 galaxies from phase 1 of ASKAP pilot observations. *Publications of the Astronomical Society of Australia*, 39:e059, 2022.

Nathan Deg and Kristine Spekkens. MCG guide, 2023a. URL https://github.com/CIRADA-Tools/MCGSuite/blob/master/Documentation/MCG_Guide.pdf.

Nathan Deg and Kristine Spekkens. Make Galaxy Guide, 2023b. URL https://github.com/CIRADA-Tools/MCGSuite/blob/master/Documentation/MakeGalaxyGuide.pdf.

Ahmed Elagali, Lister Staveley-Smith, Jonghwan Rhee, OI Wong, Albert Bosma, Tobias Westmeier, Barbel S Koribalski, G Heald, BQ For, D Kleiner, et al. WALLABY early science–iii. an HI study of the spiral galaxy NGC 1566. *Monthly Notices of the Royal Astronomical Society*, 487(2):2797–2817, 2019.

Bruce G Elmegreen and Debra Meloy Elmegreen. Properties of barred spiral galaxies. *The Astrophysical Journal*, 288:438–455, 1985.

BQ For, L Staveley-Smith, T Westmeier, M Whiting, SH Oh, B Koribalski, J Wang, OI Wong, G Bekiaris, L Cortese, et al. WALLABY early science-v. ASKAP HI imaging of the lyon group of galaxies 351. *Monthly Notices of the Royal Astronomical Society*, 489(4):5723–5741, 2019.

Filippo Fraternali, Renzo Sancisi, and Peter Kamphuis. A tale of two galaxies: light and mass in NGC 891 and NGC 7814. *Astronomy & Astrophysics*, 531: A64, 2011.

I García-Ruiz, R Sancisi, and Konrad Kuijken. Neutral hydrogen and optical observations of edge-on galaxies: Hunting for warps. *Astronomy & Astrophysics*, 394(3):769–789, 2002.

Riccardo Giovanelli, Martha P Haynes, Brian R Kent, Philip Perillat, Amelie Saintonge, Noah Brosch, Barbara Catinella, G Lyle Hoffman, Sabrina Stierwalt, Kristine Spekkens, et al. The arecibo legacy fast alfa survey. i. science goals, survey design, and strategy. *The astronomical journal*, 130(6):2598, 2005.

Martha P Haynes, Riccardo Giovanelli, Brian R Kent, Elizabeth AK Adams, Thomas J Balonek, David W Craig, Derek Fertig, Rose Finn, Carlo Giovanardi, Gregory Hallenbeck, et al. The Arecibo Legacy Fast ALFA Survey: The ALFALFA Extragalactic HI source Catalog. *The Astrophysical Journal*, 861(1):49, 2018.

AW Hotan, JD Bunton, AP Chippendale, M Whiting, J Tuthill, VA Moss, D McConnell, SW Amy, MT Huynh, JR Allison, et al. Australian square kilometre array pathfinder: I. system description. *Publications of the Astronomical Society of Australia*, 38:e009, 2021.

Gyula IG Jozsa, Franz Kenn, Uli Klein, and Tom A Oosterloo. Kinematic modelling of disk galaxies-i. a new method to fit tilted rings to data cubes. *Astronomy & Astrophysics*, 468(2):731–774, 2007.

Franz Daniel Kahn and Lodewijk Woltjer. Intergalactic matter and the galaxy. *The Astrophysical Journal*, 130:705, 1959.

P. Kamphuis, G. I. G. Józsa, S-.H. Oh, K. Spekkens, N. Urbancic, P. Serra, B. S. Koribalski, and R.-J. Dettmar. Automated kinematic modelling of warped galaxy discs in large HI surveys: 3D tilted-ring fitting of HI emission cubes. *Monthly Notices of the Royal Astronomical Society*, 452(3):3139–3158, 07 2015. ISSN 0035-8711. doi: 10.1093/mnras/stv1480. URL https://doi.org/10.1093/mnras/stv1480.

Dane Kleiner, Barbel S Koribalski, Paolo Serra, Matthew T Whiting, Tobias Westmeier, OI Wong, P Kamphuis, Attila Popping, Georgios Bekiaris, Ahmed Elagali, et al. WALLABY early science–iv. ASKAP HI imaging of the nearby galaxy IC 5201. *Monthly Notices of the Royal Astronomical Society*, 488(4):5352–5369, 2019.

Bärbel S Koribalski. The Local Volume HI Survey (LVHIS). In *Galaxies in Isolation: Exploring Nature Versus Nurture*, volume 421, page 137, 2010.

Bärbel S Koribalski, Lister Staveley-Smith, Tobias Westmeier, Paolo Serra, Kristine Spekkens, OI Wong, Karen Lee-Waddell, CDP Lagos, Danail Obreschkow, Emma V Ryan-Weber, et al. Wallaby–an SKA pathfinder HI survey. *Astrophysics and Space Science*, 365:1–35, 2020.

Davor Krajnovic, Michele Cappellari, P Tim De Zeeuw, and Yannick Copin. Kinemetry: a generalization of photometry to the higher moments of the line-of-sight velocity distribution. *Monthly Notices of the Royal Astronomical Society*, 366(3):787–802, 2006.

Michiel Kregel, Pieter C Van Der Kruit, and Richard de Grijs. Flattening and truncation of stellar discs in edge-on spiral galaxies. *Monthly Notices of the Royal Astronomical Society*, 334(3):646–668, 2002.

Karen Lee-Waddell, Barbel S Koribalski, Tobias Westmeier, Ahmed Elagali, BQ For, D Kleiner, JP Madrid, A Popping, TN Reynolds, J Rhee, et al. WALLABY early science–ii. the NGC 7232 galaxy group. *Monthly Notices of the Royal Astronomical Society*, 487(4):5248–5262, 2019.

Evan S Levine, Leo Blitz, and Carl Heiles. The vertical structure of the outer Milky Way HI disk. *The Astrophysical Journal*, 643(2):881, 2006.

Colin Lewis. *Testing Photometric and Kinematic Algorithms to predict Next-Generation Telescope Survey Statistics*. PhD thesis, Queen's University (Canada), 2019.

J McMullin, P Diamond, A McPherson, R Laing, P Dewdney, A Casson, L Stringhetti, N Rees, T Stevenson, M Lilley, et al. The square kilometre array project. In *Ground-based and airborne telescopes viii*, volume 11445, pages 215–232. SPIE, 2020.

J McMullin, P Diamond, M Caiazzo, A Casson, T Cheetham, P Dewdney, R Laing, B Lewis, A Schinckel, L Stringhetti, et al. The square kilometre array project update. In *Ground-based and Airborne Telescopes IX*, volume 12182, pages 263–271. SPIE, 2022.

Se-Heon Oh, Lister Staveley-Smith, Kristine Spekkens, Peter Kamphuis, and Bärbel S Koribalski. 2D bayesian automated tilted-ring fitting of disc galaxies in large HI galaxy surveys: 2DBAT. *Monthly Notices of the Royal Astronomical Society*, 473(3):3256–3298, 2018.

Tom Oosterloo, Filippo Fraternali, and Renzo Sancisi. The cold gaseous halo of NGC 891. *The Astronomical Journal*, 134(3):1019, 2007.

EC Ostriker and JJ Binney. Warped and tilted galactic discs. *Monthly Notices of the Royal Astronomical Society*, 237(3):785–798, 1989.

Anton Pannekoek. *A history of astronomy*. Courier Corporation, 1989.

William H Press, Saul A Teukolsky, William T Vetterling, and Brian P Flannery. *Numerical recipes in C++*. Cambridge University Press, 2nd edition, 1992.

Vladimir Reshetnikov and Francoise Combes. Statistics of optical warps in spiral disks. *arXiv preprint astro-ph/9806114*, 1998.

Vladimir Reshetnikov and Françoise Combes. Spiral galaxies with large optical warps. *Astronomy and Astrophysics Supplement Series*, 138(1):101–107, 1999.

Tristan N Reynolds, Tobias Westmeier, Lister Staveley-Smith, Ahmed Elagali, Bi-Qing For, Dane Kleiner, Baerbel S Koribalski, Karen Lee-Waddell, Juan P Madrid, Attila Popping, et al. WALLABY early science–i. the NGC 7162 galaxy group. *Monthly Notices of the Royal Astronomical Society*, 482 (3):3591–3608, 2019.

DH Rogstad, IA Lockhart, and MCH Wright. Aperture-synthesis observations of HI in the galaxy M83. *The Astrophysical Journal*, 193:309–319, 1974.

Huub Röttgering. LOFAR, a new low frequency radio telescope. *New astronomy reviews*, 47(4-5):405–409, 2003.

Iñigo García Ruiz. *Warps in disk galaxies*. University Library Groningen, 2001.

ML Sanchez-Saavedra, E Battaner, and E Florido. Frequency of warped spiral galaxies at visible wavelengths. *Monthly Notices of the Royal Astronomical Society*, 246:458, 1990.

ML Sánchez-Saavedra, E Battaner, A Guijarro, M López-Corredoira, and N Castro-Rodríguez. A catalog of warps in spiral and lenticular galaxies in the southern hemisphere. *Astronomy & Astrophysics*, 399(2):457–467, 2003.

Paolo Serra, Tobias Westmeier, Nadine Giese, Russell Jurek, Lars Flöer, Attila Popping, Benjamin Winkel, Thijs van der Hulst, Martin Meyer, Bärbel S Koribalski, et al. SOFIA: a flexible source finder for 3D spectral line data. *Monthly Notices of the Royal Astronomical Society*, 448(2):1922–1929, 2015.

Dorota M Skowron, Jan Skowron, Przemek Mróz, Andrzej Udalski, Paweł Pietrukowicz, Igor Soszyński, Michał K Szymański, Radosław Poleski, Szymon Kozłowski, Krzysztof Ulaczyk, et al. A three-dimensional map of the milky way using classical Cepheid variable stars. *Science*, 365(6452):478–482, 2019.

Kristine Spekkens and Riccardo Giovanelli. The structure of rapidly rotating late-type spiral galaxies. i. photometry, HI, and optical kinematics. *The Astronomical Journal*, 132(4):1426, 2006.

Kristine Spekkens and JA Sellwood. Modeling noncircular motions in disk galaxies: Application to NGC 2976. *The Astrophysical Journal*, 664(1):204, 2007.

EM Di Teodoro and Filippo Fraternali. 3D BAROLO: a new 3D algorithm to derive rotation curves of galaxies. *Monthly Notices of the Royal Astronomical Society*, 451(3):3021–3033, 2015.

JM Van der Hulst, JP Terlouw, KG Begeman, W Zwitser, and PR Roelfsema. The groningen image processing system, GIPSY. In *Astronomical Data Analysis Software and Systems I*, volume 25, page 131, 1992.

PC Van der Kruit. Truncations of stellar disks and warps of HI-layers in edge-on spiral galaxies. *Astronomy & Astrophysics*, 466(3):883–893, 2007.

Fabian Walter, Elias Brinks, WJG De Blok, Frank Bigiel, Robert C Kennicutt, Michele D Thornley, and Adam Leroy. THINGS: The HI nearby galaxy survey. *The Astronomical Journal*, 136(6):2563, 2008.

Jing Wang, Bärbel S Koribalski, Paolo Serra, Thijs van der Hulst, Sambit Roychowdhury, Peter Kamphuis, and Jayaram N. Chengalur. New lessons from the HI size–mass relation of galaxies. *Monthly Notices of the Royal Astronomical Society*, 460(2):2143–2151, 2016.

T Westmeier, N Deg, K Spekkens, TN Reynolds, AX Shen, S Gaudet, S Goliath, MT Huynh, P Venkataraman, X Lin, et al. Wallaby pilot survey: Public release of HI data for almost 600 galaxies from phase 1 of ASKAP pilot observations. *Publications of the Astronomical Society of Australia*, 39: e058, 2022.

OI Wong, ARH Stevens, BQ For, T Westmeier, M Dixon, SH Oh, GIG Józsa, TN Reynolds, K Lee-Waddell, J Roman, et al. WALLABY pre-pilot survey: two dark clouds in the vicinity of NGC 1395. *Monthly Notices of the Royal Astronomical Society*, 507(2):2905–2921, 2021.

Martin A Zwaan, Martin J Meyer, Rachel L Webster, Lister Staveley-Smith, Michael J Drinkwater, David G Barnes, Raghir Bhathal, WJG De Blok, Michael J Disney, Ron D Ekers, et al. The HIPASS catalogue–ii. completeness, reliability and parameter accuracy. *Monthly Notices of the Royal Astronomical Society*, 350(4):1210–1219, 2004.